Amorphous nickel hydroxide proton conductive shell tailors local chemical environment on Pt surface for high-performance alkaline hydrogen evolution reaction

Chengzhang Wan[1,2], Zisheng Zhang[1], Juncai Dong[3], Mingjie Xu[4, 5], Heting Pu[1], Daniel Baumann[1], Zhaoyang Lin[1], Sibo Wang[1], Jin Huang[2], Aamir Hassan Shah[1], Xiaoqing Pan[4,5,6], Tiandou Hu[3], Anastassia N. Alexandrova*[1,7], Yu Huang*[2,7], Xiangfeng Duan*[1,7,]

[1]Department of Chemistry and Biochemistry, University of California, Los Angeles; California 90095, United States;[2]Department of Materials Science and Engineering, University of California, Los Angeles; California 90095, United States; [3]Beijing Synchrotron Radiation Facility, Institute of High Energy Physics, Chinese Academy of Sciences; Beijing, China; [4]Department of Materials Science and Engineering, University of California, Irvine; California 92697, United States; [5]Irvine Materials Research Institute, University of California, Irvine; California, 92697, United States; [6]Department of Physics and Astronomy, University of California, Irvine; California 92697, United State; [7]California NanoSystems Institute, University of California, Los Angeles; California 90095, United States.

**Correspondence. xduan@chem.ucla.edu, yhuang@seas.ucla.edu, ana@chem.ucla.edu*

In analogy to natural enzymes, an elaborated design of catalytic systems with a specifically tailored local chemical environment could substantially improve reaction kinetics, effectively combat catalyst poisoning effect and boost catalyst lifetime under unfavorable reaction conditions. Herein, we report a unique design of "$Ni(OH)_2$-clothed Pt-tetrapods" with an amorphous $Ni(OH)_2$ shell as a water dissociation catalyst and a proton conductive layer to ensure abundant proton supply while isolating the Pt core from bulk alkaline electrolyte and rejecting undesired poisoning species. This design creates a favorable local chemical environment with efficient proton supply to the active Pt sites, resulting in acidic-like HER kinetics with a lowest Tafel slope of 27 mV/decade and a record-high specific activity and mass activity in alkaline electrolyte. The proton conductive $Ni(OH)_2$ shell effectively rejects impurity ions and retards the Oswald ripening, endowing a high tolerance to solution impurities and long-term durability that is difficult to achieve in the naked Pt-catalysts. The markedly improved alkaline HER activity and durability promise

an attractive catalyst material for alkaline water electrolyzers and renewable chemical fuel generation.

Water electrolysis is of increasing interest for converting intermittent renewable electricity (from solar cells and windmills) into high purity hydrogen. The electrochemical water-splitting reaction is comprised of two half-reactions: the cathodic hydrogen evolution reaction (HER) and anodic oxygen evolution reaction (OER). In general, the HER and OER display distinct kinetics in acidic and basic electrolytes and often require costly platinum group metal (PGM) catalysts. Platinum (Pt) is regarded as the best element to catalyze HER for its optimal hydrogen binding energy (HBE).[1-6] In particular, the Pt catalysts feature a rather small overpotential for HER in the acidic condition where the cathodic HER is usually regarded as a trivial challenge. However, for the complete water electrolysis, the anodic OER in the acidic condition is considerably more challenging and often features large overpotential and limited durability even with the most advanced design of PGM catalysts.[7] On the other hand, the OER in the alkaline condition is much more friendly and can be readily facilitated with non-precious metal (Ni, Fe, Co, etc.) oxide/hydroxide catalysts, offering considerable kinetic and cost benefits.[8] With the continued development of anion exchange membrane (AEM) of lower resistance and lower hydrogen diffusivity,[9] alkaline electrolysis is becoming an increasingly attractive alternative for commercial electrolyzers.[10,11]

However, the HER kinetics in the alkaline condition is considerably slower. Even with the Pt catalysts, the HER rate is orders of magnitude lower than that in the acidic electrolyte because of the sluggish water dissociation step and the poor proton supply rate (Extended Data Fig. 1).[12] Therefore, **unlike the commonly perceived "easy" HER in the acidic electrolyte, the HER in the alkaline condition represents a major challenge for alkaline water electrolyzers**.[13,14] Considerable efforts have been placed on tailoring the Pt active sites to optimize HBE and HER kinetics. **Beyond the active sites**, the local chemical species can compete for adsorption for active sites, inactivate (poison) the catalytic sites, or profoundly affect the mass transfer of feedstocks/products.[15,16] Additionally, catalysts are inherently dynamic materials whose structures may evolve continuously during the adsorption of reactants and desorption of products, which could dictate the catalyst stability and lifetime.

In general, the local chemical environment plays a fundamental role in determining the reaction pathway and kinetics on the catalytic surface. A practical water electrolysis requires the concerted supply of the reactants and removal of the products under specific operating conditions

to achieve high activity, tolerance to impurities in water, and long lifetime. To this end, **a comprehensive approach that integrates electrocatalytic active site design with rational strategies to manipulate nanoscale mass/charge transport, ion separation, or structural evolution is critical for designing high-performing electrocatalysts that can facilitate efficient electron transfer and chemical transformations under practical conditions. This is analogous to the natural enzymes where precisely tailored micro-environment works in concert with the active sites to ensure superior activity, selectivity, and durability under practical solution conditions.** Such an elaborate design is particularly important for alkaline water electrolysis where the local chemical environment near the active Pt sites in alkaline electrolytes is far more complex than that in an acidic electrolyte due to the limited proton supply rate, competitive adsorption of positively charged alkali metal cations (*vs.* protons) or other undesirable strong binding impurities (e.g., Cl^-) that could posizon the catalytic sites.

Surface decoration has been recognized as an effective approach for tailoring the local chemical environment near the active sites. For example, the decoration of crystalline NiO or NiS_x particles on Pt surface has been reported to improve HER specific activity (SA, activity normalized by electrochemical surface area: ECSA) in the alkaline electrolyte,[17,18] which has been mostly attributed to enhanced water dissociation kinetics facilitated by the Ni species. However, such crystalline Ni species are less permeable to protons and partly block the surface active sites (Extended Data Fig. 2) to reduce proton-accessible ECSA and compromise the overall mass activity (MA, activity normalized by mass loading);[5] Additionally, the protons generated from Ni-catalyzed water dissociation could be rapidly consumed within ~1 nm (See Supplementary Note 1) through reassociation with the abundant hydroxyl in alkaline electrolyte. Thus, only a small fraction of Pt sites in close proximity of the decorated Ni species can benefit from the improved water dissociation kinetics on decorated Ni species, while most Pt sites farther away from Ni species are barely impacted (Extended Data Fig. 2). In this way, although the surface decoration with the crystalline Ni species could facilitate the water dissociation and partly accelerate the HER kinetics, **most of the surface Pt sites in such decorated catalysts remain exposed to the bulk alkaline electrolyte, and the HER kinetics largely retain the alkaline HER characteristics with the Vomer- and Heyrovsky-step limited kinetics**

(Extended Data Table 1). Moreover, the exposed Pt surface sites could undergo severe Oswald ripening during HER and gradually lose the designed nanostructure and the original activity.

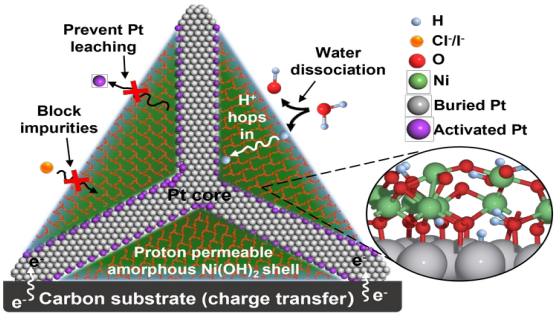

Figure 1| "$Ni(OH)_2$-clothed Pt-tetrapod" with the proton conductive amorphous $Ni(OH)_2$ to tailor local chemical environment for optimum HER in bulk alkaline electrolyte: (i) the "**$Ni(OH)_2$-clothed** Pt-tetrapod" structure offers an ideal geometry for isolating most of the Pt surface sites from the bulk alkaline electrolyte and rejecting undesired poisoning species while allowing the less encapsulated "feet" to make robust electrical contacts with the carbon support for efficient electron transport to the catalytic sites; (ii) the amorphous $Ni(OH)_2$ shell functions as an effective water dissociation catalyst and a **low-barrier proton conductive layer** to ensure efficient proton supply to the interfacial Pt sites, creating a proton-enriched local environment and fundamentally altering the HER to kinetics to the acidic-like Tafel-step limited pathway; (iii) the proton conductive $Ni(OH)_2$ shell effectively **rejects impurity ions** and **retards Oswald ripening** process, endowing a high tolerance to water impurities and long-term durability not attainable in the naked Pt-catalysts.

Herein we report a unique design of "**$Ni(OH)_2$-clothed Pt-tetrapod**" core/shell nanostructure [Pt_{tet}@$Ni(OH)_2$] to create a local chemical environment that can provide efficient proton (H^+) supply to the Pt active sites and greatly boost HER performance in alkaline medium (Fig. 1B). The designed [Pt_{tet}@$Ni(OH)_2$] consists of a Pt nano-tetrapod (Pt_{tet}) core as the HER catalyst and an amorphous $Ni(OH)_2$ shell as the water dissociation (WD) catalysts and proton conductive layer. In particular, the hydrogen-bond framework in the amorphous $Ni(OH)_2$ layer stabilizes the intermediate state of the WD step and facilitates water dissociation into OH^- and H^+, with OH^- diffusing into the alkaline electrolyte and the H^+ efficiently transporting to the Pt surface through the amorphous $Ni(OH)_2$ matrix following a low-barrier cascade pathway (Grotthuss-like mechanism).[19,20] The rapid water dissociation and low-barrier proton permeation through amorphous $Ni(OH)_2$ matrix provide abundant proton supply to the active Pt sites,[19,20] fundamentally altering the HER kinetics to the acidic-like Tafel step limited pathway. Meanwhile, the tetrapod feet feature intrinsically thinner $Ni(OH)_2$ decoration layer and

geometrically and electrically favorable contacting point with the carbon support[21] to ensure efficient electron transfer to the catalytic sites for electrocatalytic process. Additionally, the encapsulation by the proton conductive $Ni(OH)_2$ efficiently rejects water impurity ions (e.g., Cl^- and I^-) and suppresses Pt atom leaching, leading to significantly enhanced tolerance to water impurities, long-term operation durability, and the overall catalyst lifetime. Together, the designed $Pt_{tet}@Ni(OH)_2$ catalysts display acidic-like HER kinetics, achieving a lowest Tafel slope of 27 mV/dec, a record-high specific activity, and mass activity (27.7 ± 0.5 mA/cm^2 Pt and 13.4 ± 0.4 A/mg$_{Pt}$ at -70 mV vs. reversible hydrogen electrode: RHE) in alkaline electrolyte, along with excellent durability and tolerance towards halide anions not attainable in conventional naked Pt catalysts.

Structure characterizations of $Pt_{tet}@Ni(OH)_2$

The $Pt_{tet}@Ni(OH)_2$ nanoparticles were prepared through a facile one-pot synthesis (see Methods). Transmission electron microscopy (TEM) studies reveal the resulting nanoparticles exhibit uniformly dispersed tetrahedral shapes (Fig. 2a). The high-angle-annular-dark-field scanning TEM (HAADF-STEM) and energy-dispersive X-ray spectroscopy (EDS) mapping studies (Fig. 2b) reveal the tetrahedral nanoparticle is composed of a Pt tetrapod core encapsulated in a Ni-containing shell to form an overall tetrahedral shape, with a total Pt/Ni atomic ratio of 1.0:2.3 (Extended Data Fig. 3). High-resolution STEM images reveal the Pt tetrapods grow along <111> directions (Extended Data Fig. 4), while the Ni-containing shell shows no apparent crystalline order, indicating an amorphous nature (Extended Data Fig. 5). X-ray photoelectron spectroscopy (XPS) studies show Pt emission peaks can be assigned to Pt (0) with minor Pt(+2) species; while that of Ni are consistent with $Ni(OH)_2$ (Extended Data Fig. 6).[22-26] X-ray diffraction (XRD) studies show all diffraction peaks can be assigned to face-centered cubic Pt (Extended Data Fig. 6), with no apparent diffraction peaks for nickel species,[27-29] further confirming the amorphous nature of the $Ni(OH)_2$ shell. It is interesting to note that STEM EDS mapping studies (Fig. 2b) indicate the Pt-tetrapod body is well encapsulated by the amorphous $Ni(OH)_2$ shell, while the Pt-tetrapods feet (tips) are less encapsulated. Previous studies suggested that the Ni adatoms tend to fill the concave sites of the Pt multi-pod structure following a step-site induced layer-by-layer deposition process.[30] Such a concave-site filling process on Pt-tetrapods would eventually saturate all concave sites of four (111) faces, forming

tetrahedral structures with intrinsically less encapsulated tetrapod feet on four convex corners, producing a unique structure of "**$Ni(OH)_2$-clothed Pt-tetrapods**", which is **ideally suited for isolating most of the Pt surface from the bulk alkaline electrolyte while allowing the less encapsulated tetrapod-feet to make robust electrical contacts with the carbon support for efficient electron transport to the catalytic sites** (Fig. 1).

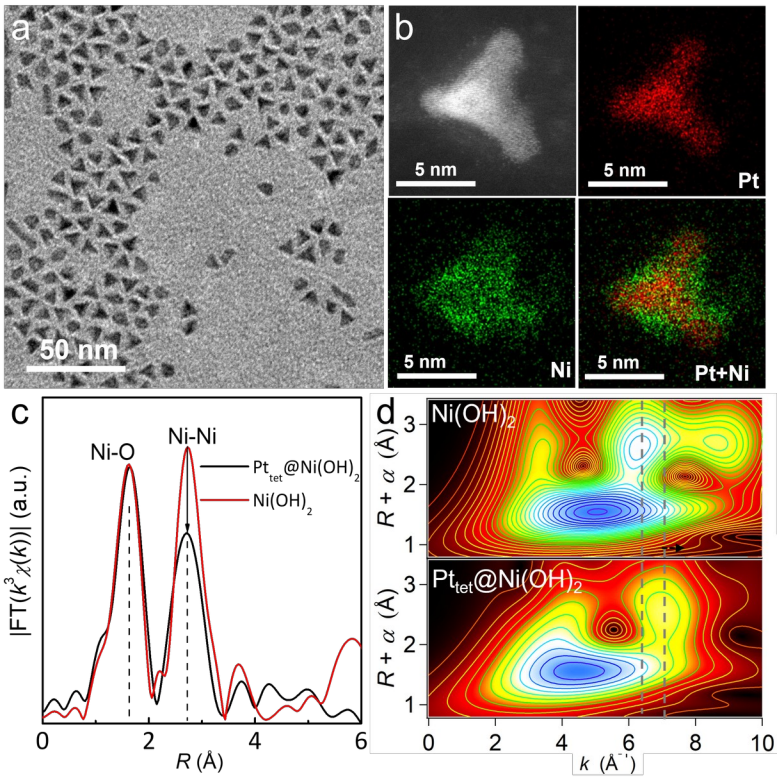

Figure 2| Structural characterizations of Pt_{tet}@$Ni(OH)_2$ nanocatalysts. a, The TEM image of Pt_{tet}@$Ni(OH)_2$. **b,** HAADF image of Pt_{tet}@$Ni(OH)_2$, and STEM-EDS mapping images of Pt, Ni, and Pt+Ni. **c,** Ni K edge EXAFS-FT signals of Pt_{tet}@$Ni(OH)_2$ and α-$Ni(OH)_2$. The significantly lower peak intensity and broader peak width at half maximum for the Ni-Ni peak in Pt_{tet}@$Ni(OH)_2$ *vs.* crystalline α-$Ni(OH)_2$ reference indicate the amorphous nature of the $Ni(OH)_2$ shell. **d,** Wavelet transform (WT) for the Ni k^3-weighted EXAFS signals of α-$Ni(OH)_2$ and Pt_{tet}@$Ni(OH)_2$. The positive shift of the Ni-Ni coordination signal from 6.4 to 7.0 $Å^{-1}$) in the *k*-space indicates Ni is also coordinated with a heavier element, which should be the Pt.

The Fourier transform (FT) extended X-ray absorption fine structure (EXAFS) signal of Pt_{tet}@$Ni(OH)_2$ exhibits a major peak of Ni-O at 1.66 Å, and a second major peak of Ni-Ni at 2.69 Å (Fig. 2c). We note that the corresponding peak intensities for the Ni-Ni peaks (second coordination sphere) are considerably lower than that of standard α-$Ni(OH)_2$, suggesting abundant Ni defects in the $Ni(OH)_2$ shell and the high level of structural disorder. Additionally, the Pt_{tet}@$Ni(OH)_2$ features a notably broader Ni-Ni peak at half maximum with a considerably

larger Debye-Waller factor than that of the standard crystalline α-$Ni(OH)_2$ (Extended Data Table 2), further suggesting the amorphous nature of the $Ni(OH)_2$ in Pt_{tet}@$Ni(OH)_2$ and consistent with the results obtained in TEM and XRD studies. The X-ray absorption near edge structure (XANES) spectra of Ni K-edge and Pt L_3-edge suggest that the oxidation state of Ni is slightly lower than +2, while the oxidation state of Pt is slightly higher than 0 (Extended Data Fig. 7 and 8), indicating a partial charge transfer from Pt to the $Ni(OH)_2$ at the interface. This charge transfer is also confirmed by the density functional theory (DFT) calculations of the Bader charge of interfacial Pt and Ni atoms in the next section.

EXAFS wavelet transform (WT) analysis is powerful for discriminating the backscattering atoms. The main signal of Ni-Ni coordination lies at 6.4 $Å^{-1}$ in the k-space for standard $Ni(OH)_2$ reference (Fig. 2D), which shifts towards higher values (7.0 $Å^{-1}$) for Pt_{tet}@$Ni(OH)_2$, indicating the existence of Ni-Pt coordination. This is also consistent with the negative shift of Pt-Pt *k* value observed in Pt-L_3 edge EXAFS-WT analysis for Pt_{tet}@$Ni(OH)_2$ (Extended Data Fig. 9). Based on the EXAFS-WT results, the EXAFS spectrum of the Pt_{tet}@$Ni(OH)_2$ was analyzed by quantitative least-square EXAFS curve-fitting using backscattering paths of Ni-Pt, Ni-Ni, and Ni-O (Extended Data Fig. 10 and Table 2 and 3). The best-fitting results show that the bonding distance of Ni-Pt coordination is 3.10 Å, considerably larger than the 2.66 Å Ni-Pt distance in the PtNi alloy, indicating that the Ni and Pt atoms in Pt_{tet}@$Ni(OH)_2$ are likely bridged by O atoms. This is further confirmed by the DFT studies in the following section. Proton permeability through $Ni(OH)_2$ shell and acidic-like local environment on Pt surface

Proton permeability through $Ni(OH)_2$ shell and acidic-like local environment on Pt surface

Since it is difficult to directly evaluate the proton permeability through the amorphous $Ni(OH)_2$ layer, we have compared cyclic voltammetry (CV) characteristics of Pt_{tet}@$Ni(OH)_2$ and the naked Pt_{tet} in the alkaline electrolyte to evaluate the proton accessibility of the $Ni(OH)_2$ encapsulated Pt core in Pt_{tet}@$Ni(OH)_2$ (Fig. 3a). The naked Pt_{tet} was obtained by completely etching the $Ni(OH)_2$ shell in the acidic electrolyte (Extended Data Fig. 4). Based on the CV curves, the proton-accessible ECSA can be quantified by the integration of the hydrogen desorption region (0.05-0.45 V vs. RHE). Interestingly, the ECSA of the original Pt_{tet}@$Ni(OH)_2$ with full $Ni(OH)_2$ encapsulation is about 80% of the naked Pt_{tet} obtained after completely removing the surface $Ni(OH)_2$, indicating that **the Pt sites in the Pt_{tet}@$Ni(OH)_2$ coreshell**

structures are mostly accessible to the H^+ even with the encapsulation by the $Ni(OH)_2$ shell, suggesting the proton permeability of the $Ni(OH)_2$ shell.

Most Pt catalysts typically exhibit notably different CV in acidic or alkaline electrolytes with highly distinct behavior in the hydrogen desorption region (H_{upd}) region due to distinct local proton concentration and different hydrogen adsorption/desorption potential.[28,31,32] Indeed, the naked Pt_{tet} shows a rather different CV behavior in the alkaline *vs.* acidic conditions (Fig. 3b), consistent with previous studies. On the other hand, it is interesting to note that **the CV curves of the Pt_{tet}@$Ni(OH)_2$ in the alkaline electrolyte show rather similar behavior in the H_{upd} region to that of the naked Pt_{tet} in the acidic electrolyte (Fig. 3c), indicating a largely comparable proton supply near the Pt sites in Pt_{tet}@$Ni(OH)_2$ even in bulk alkaline electrolyte**.

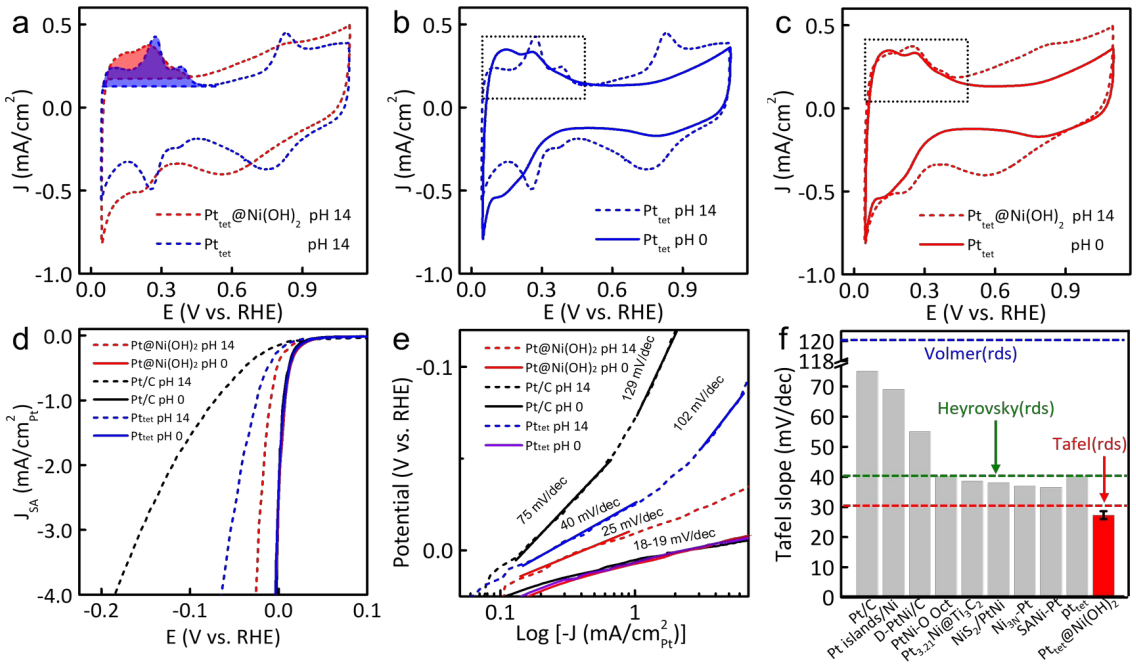

Figure 3| Electrochemical characterizations of Pt_{tet}@$Ni(OH)_2$ nanocatalysts. a, The CV of the Pt_{tet}@$Ni(OH)_2$ and naked Pt_{tet} in 1.0 M KOH. The Pt ECSA of the Pt_{tet}@$Ni(OH)_2$ with full $Ni(OH)_2$ shell is about ~80 % of the ECSA of the naked Pt_{tet}, confirming the proton permeability through the amorphous $Ni(OH)_2$ shell. **b,** The CV curves of the naked Pt_{tet} under pH 0 and 14 show distinct characteristics in the hydrogen adsorption/desorption region. **c,** The CV curves of Pt_{tet}@$Ni(OH)_2$ under pH 0 and 14 show highly comparable characteristics in hydrogen adsorption/desorption region, indicating a largely comparable proton supply near the Pt sites in Pt_{tet}@$Ni(OH)_2$ even in bulk alkaline electrolyte. **d,** Polarization curves (specific activity) of Pt_{tet}@$Ni(OH)_2$, Pt_{tet}, and Pt/C in pH 0 and 14, respectively. **e,** Tafel slopes of Pt_{tet}@$Ni(OH)_2$, Pt_{tet} and Pt/C pH 0 and 14, respectively. **f,** Comparison of the Tafel slopes of Pt_{tet}@$Ni(OH)_2$ with the state-of-the-art alkaline HER catalysts. The dotted lines represent the

Tafel slopes determined by three distinct rate-determining steps (rds): Volmer step (blue); Heyrovsky step (green), and Tafel step (red). All previous studies of Pt or modified Pt catalysts show a Tafel slope of ~40 mV/dec or above in alkaline electrolytes, consistent with a Volmer step or Heyrovsky limited mechanism, while the Tafel slope achieved with our Pt_{tet}@$Ni(OH)_2$ catalysts is below 29.6 mV/dec, comparable to the typical values observed in the acidic electrolyte, suggesting abundant proton supply near Pt surface in our unique design of Pt_{tet}@$Ni(OH)_2$ catalysts despite the bulk alkaline electrolyte.

The efficient proton supply could lead to considerably improved HER kinetics. To this end, we have conducted linear scan voltammetry (LSV) and compared the HER polarization curves (normalized by hydrogen desorption area) of Pt_{tet}@$Ni(OH)_2$, naked $Pt_{tet,}$ and Pt/C in pH 14 and pH 0 (Fig. 3d). Expectedly, the Pt/C under pH 14 shows a markedly lower current than under pH 0. Similarly, the naked Pt_{tet} without the $Ni(OH)_2$ shell also shows considerably lower HER current in the alkaline electrolytes than that in acidic conditions. In contrast, **the Pt_{tet}@$Ni(OH)_2$ shows a much more comparable HER polarization curve between the alkaline condition and the acidic condition, further suggesting a similar local chemical environment regardless of the entirely different bulk electrolytes**. Additionally, the uninterrupted increase of the HER current from the Pt_{tet}@$Ni(OH)_2$ catalysts during the cathodic LSV scan (Fig. 3d) indicates that the amorphous $Ni(OH)_2$ layer is also H_2 permeable.

These specific HER kinetics can be highlighted by the Tafel slope analysis. The HER reaction follows three basic steps, with distinct rate-determining steps (rds) and Tafel slopes:[12]

Volmer step: $H_3O^+ + e^- \rightarrow H_{ad} + H_2O$ (acidic electrolyte)

Or: $H_2O + e^- \rightarrow H_{ad} + OH^-$ (alkaline electrolyte)

Heyrovsky step: $H_{ad} + H_3O^+ + e^- \rightarrow H_2\uparrow + H_2O$ (acidic electrolyte)

Or: $H_{ad} + H_2O + e^- \rightarrow H_2\uparrow + OH^-$ (alkaline electrolyte)

Tafel step: $2H_{ad} \rightarrow H_2\uparrow$ (both acidic and alkaline electrolyte)

Depending on the electrolyte conditions, we expect distinct reaction kinetics. In the acidic electrolyte, the sufficient H^+ supply ensures a Tafel-step limited HER pathway, with the Tafel step as the rds and an ideal Tafel slope of 29.6 mV/dec. In the alkaline electrolyte where the H^+ is supplied by water dissociation, the HER reaction typically follows Volmer- or Heyrovsky-step limited pathway, with the Volmer step or Heyrovsky step as the rds, and ideal Tafel slopes of 118.4 and 39.5 mV/dec, respectively.

The Pt/C, naked $Pt_{tet,}$ and Pt_{tet}@$Ni(OH)_2$ show a low and comparable Tafel slope of around 18-19 mV/dec at pH 0 (Fig. 3e), consistent with previous reports in the acidic environment and the well-accepted HER mechanism with the Tafel-step limited pathway described above.[33-36] The smaller than 29.6 mV/dec Tafel slope is possibly ascribed to the backward HOR reaction with H_2 *in-situ* generated on the Pt surface at a small HER overpotential regime and has also been commonly observed in previous works.[33-36] On the other hand, the Pt/C, naked $Pt_{tet,}$ and Pt_{tet}@$Ni(OH)_2$ show distinct Tafel slopes of 75-129 mV/dec, 40-102 mV/dec, and 27 mV/dec at pH 14 (Fig. 3e). We note that Tafel slope derivation can be tricky in some situations,[37,38] and have taken extra caution in deriving the Tafel slopes (See Supplementary Note 2) to ensure a fair and robust comparison. The much higher Tafel slopes observed for Pt/C and Pt_{tet} at pH 14 are consistent with the Volmer or Heyrovsky limited kinetics expected in the alkaline electrolyte, **while the much lower Tafel slope of 27 mV/dec observed for Pt_{tet}@$Ni(OH)_2$ at pH 14 suggests a distinct Tafel step limited mechanism more similar to that in an acidic environment.**[39-42] Indeed, a closer comparison of the HER activity of Pt_{tet}@$Ni(OH)_2$ in pH 14 with that of Pt/C under pH 0-3 condition indicate that the HER activity of Pt_{tet}@$Ni(OH)_2$ in pH 14 is largely comparable to that of Pt/C under pH 1 (Extended Data Fig. 11). **These HER polarization analyses further suggest that the Pt sites in Pt_{tet}@$Ni(OH)_2$ feature a proton supply rate closed to that of an acidic environment (pH 1-2), consistent with the CV analyses discussed above**.

It is interesting to note that the HER Tafel slope of 27 mV/dec achieved with Pt_{tet}@$Ni(OH)_2$ represents the lowest value achieved in the alkaline electrolyte, which is notably lower than those achieved previously with Pt or modified Pt catalysts in alkaline conditions (Fig. 3f).[4,43-48] Although it has been well reported that the surface decoration with Ni species may facilitate the water dissociation and partly accelerate the HER kinetics on Pt, **most of the surface Pt sites in such decorated catalysts remain exposed to the bulk alkaline electrolyte, and the HER kinetics largely retain the alkaline HER characteristics with the Vomer and Heyrovsky step limited kinetics and an overall Tafel slope ~40 mV/dec or larger** (see Extended Data Table 1). In contrast, a full encapsulation of Pt surface with a proton permeable amorphous $Ni(OH)_2$ in our Pt_{tet}@$Ni(OH)_2$ core-shell catalysts isolates most active Pt sites from bulk alkaline electrolyte

while ensuring sufficient proton supply to all Pt sites, thus fundamentally altering the HER pathway to acidic-like Tafel-step limited kinetics.

Theoretical study on the water dissociation and proton transfer at Pt/Ni(OH)$_2$ interface

To understand the intriguing acidic-like HER kinetics at Pt/Ni(OH)$_2$ interface observed in our experiments, we established an atomistic model of the Pt/Ni(OH)$_2$ interface using grand canonical genetic algorithm at the DFT level (see Methods, Extended Data Fig. 12 and 13 for sampling details), and obtained a highly disordered NiO_xH_y layer over 4-layer 4x4 supercell of Pt(111) as the global minimum configuration ($Ni_{12}O_{25}H_{13}$ (Fig. 4a). The nonstoichiometric H/O ratio in the $Ni_{12}O_{25}H_{13}$ model is due to the formation of Pt-O-Ni bonds that replace part of the H atoms in the simulated model, while keeping a finite number of H-O-Ni moieties near the interface. The coordination number and the bonding length are consistent with the EXAFS results, confirming the accuracy of this model in simulating the local chemical environment (Extended Data Table 4). The non-crystalline NiO_xH_y has an outer layer that is not directly linked to Pt, and directly interfaces with bulk electrolyte; and an inner layer representing the Pt/NiO_xH_y interface. The inner layer of NiO_xH_y is directly bonded to Pt(111) via the Ni-O-Pt bonds and occasional Ni-Pt linkages, in agreement with EXAFS studies. Overall, the NiO_xH_y film contains a more flexible Ni-O framework and hydrogen bond matrix featuring a coexistence of Ni-bonded OH, adsorbed H_2O, bridging O, and bridging O-H^+ species (Fig. 4b), which is significantly different from the crystalline layered double hydroxide (LDH) where the Ni-O framework is more rigid and all the hydroxyls point normal to the basal planes of the crystalline layers.

The NiO_xH_y layer influences the electronic structure of surface Pt sites, with the Bader charges of the surface Pt atoms changing from slightly negative to positive (Extended Data Fig. 14), in agreement with the XANES results. The surface Pt atoms directly bonded to O atoms undergo the most significant charge transfer of *circa* +0.40 *e* to NiO_xH_y. The exposed Pt atoms also exhibit a slightly positive charge shift to +0.11 *e*. The reduced electron density on those exposed Pt makes them no longer able to chemisorb *H on an *fcc* site but only on the atop site. The atop H adsorption on an exposed Pt atom has ΔG_H^o of -0.14 eV, which is weaker than on the atop sites (-0.26 eV) on bare Pt(111) but still stronger than the *fcc* sites (-0.09 eV) on bare Pt(111) (see Extended Data Table 5). Considering the pH of the alkaline electrolyte, the ΔG_H of

Pt (111) atop, Pt(111) *fcc* sites, and Pt@NiO_xH_y atop sites are 0.57 eV, 0.74 eV, and 0.69 eV at pH 14. They are all on the right side of the Sabatier volcano and far away from the volcano top, resulting in a significant activity drop compared with that of the acidic condition. (Extended Data Fig. 15). The relatively small ¿ ΔG_H ∨¿ difference of 0.05 eV between Pt@NiO_xH_y atop sites and bare Pt *fcc* sites cannot fully account for the experimentally observed drastic HER activity boost in Pt@NiO_xH_y, suggesting additional factors in play.

The alkaline HER activity largely relies on the proton generation rate from WD step and the proton supply rate to the catalytic sites. There have been reports that nanostructured metal catalysts could enrich local proton concentration without affecting the nature of the active sites to enhance the HER activity.[32] Since the main H^+ source in the alkaline medium is water, we investigate the water dissociation pathways on two different NiO_xH_y sites (Fig. 4c). For the reference, water dissociation on Pt(111) has an activation barrier of 0.92 eV and a ΔG of 0.70 eV (Fig. 4c red). At the outer layer of NiO_xH_y, water gets dissociated at the 4-coordinated Ni, transferring one H^+ to a neighboring bridging O, with a lower activation barrier of 0.49 eV and a ΔG of 0.33 eV (Fig. 4c green), which is similar to the energetics of water dissociation on crystalline $Ni(OH)_2$ surface (Extended Data Fig. 16a). Note that the bridging O in Ni-O-Ni is coordinatively saturated, and the H^+ thus forms a loosely held O-H^+ bridge. The H^+ on such bridging O-H^+ in top-layer Ni could readily detach and move to other bridging O within NiO_xH_y, which is equivalent to injecting an H^+ into NiO_xH_y matrix. After the water dissociates at the unsaturated Ni sites and transfers the H^+ to the bridging O, the remaining OH^- on Ni can diffuse away from the electrode via proton exchange with nearby free water molecules to initiate a new WD catalytic cycle and maintain charge balance. Deeper into the NiO_xH_y layer, water can more readily dissociate with the assistance of the H-bonding network, by transferring H^+ to nearby bridging O, showing a lower barrier of 0.19 eV (Fig. 4c blue), 0.3 eV smaller than the case of crystalline $Ni(OH)_2$.

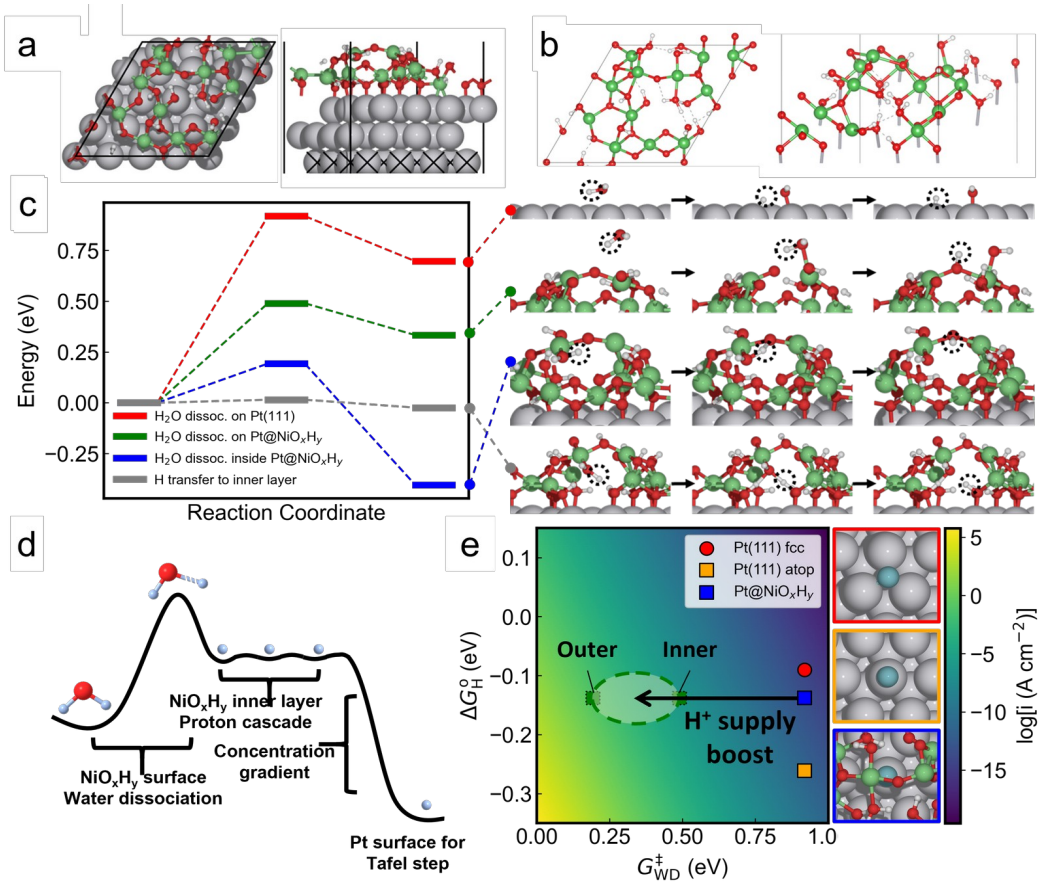

Figure 4| DFT calculations of the Pt@NiOxHy interface. a, The top and side views of the global minimum geometry of the disordered NiO_xH_y layer on Pt surface from the GCGA search. **b,** The hydrogen bond network in the NiO_xH_y layers. The Pt(111) substrate is hidden for clarity. **c,** Energy profiles of the water dissociation processes on bare Pt(111), the outer surface of Pt@NiO_xH_y, inside the NiO_xH_y matrix, and the proton transfer to the inner layer. The geometries of the initial, transition and final states are shown to the right of the diagram. Note that due to the Pt-O-Ni linkages nearby, the *fcc* sites cannot stably host an *H as on bare Pt(111), and the atop site is the only available type on Pt covered by NiO_xH_y. Atomic color code: H, white; O, red; Ni, green; Pt, grey; *H, blue. **d,** The schematic of the reaction pathway on Pt@NiO_xH_y. The water dissociates at the NiO_xH_y surface to generate protons that migrate through the H-bond network in NiO_xH_y layer to reach the ative Pt surface. **e,** HER activity colormap showing log(*i*) at the investigated HER sites as a function of ΔG‡ WD and ΔGo H. The geometries of the *H are shown on the right.

The efficient transport of protons to the interfacial Pt sites is critical for sustained HER. Our model of the Pt/$Ni(OH)_2$ interface indicates that the NiO_xH_y is non-stoichiometric and amorphous, featuring a complex H-bond network with three relevant deprotonation/protonation states including oxo, hydroxyl, and adsorbed water, in which both hydroxyl/oxo and water/hydroxyl pairs can facilitate proton transfer through protonation/deprotonation process with a rather low activation barrier of 0.02 eV (Fig. 4c) and 0.03 eV (Extended Data Fig. 17). These are in sharp contrast to the much higher barrier for intra- and inter-layer proton migration

(1.09 and 0.54 eV, respectively) in crystalline $Ni(OH)_2$ (Extended Data Fig.16 B and C), where the Ni-O framework is much more rigid and an interwoven H-bond matrix is not present. Notably, in the final state a proton transfer process in the NiO_xH_y matrix, the H^+ is located 1.24 Å and 1.15 Å from the donor and acceptor O sites, respectively, i.e., longer than a typical O-H bond (~0.98 Å) but significantly shorter than a typical O · · · H hydrogen bond (~1.97 Å). This structure is similar to the oxonium ion ($H_5O_2^+$), where the shared proton is located ~1.21 Å from the O atoms. [49] Therefore, **at the thermodynamic equilibrium state, the protons inside NiO_xH_y are delocalized between the donor and the acceptor sites, and follow the Grotthuss-type mechanism to cascade from the NiO_xH_y/electrolyte interface to the Pt/NiO_xH_y interface**.

In this picture, the water or hydroxyl near the Pt surface gets dissociated and adsorbed by Pt sites to form Pt-H, leaving a "proton-hole" (hydroxyl or oxo) in the interfacial NiO_xH_y, which provides the effective driving force for the H^+ generated from the water dissociation at the NiO_xH_y/electrolyte interface to cascade inwards to reach the interfacial Pt sites through H-bond network in NiO_xH_y (Fig. 4d). Considering the substantial size difference and more substantial structural reorganization needed to accommodate water or OH^- transfer in the NiO_xH_y matrix, the direct transfer of OH^- or H_2O would be considerably more sluggish. In this way, **the NiO_xH_y layer behaves as a proton selective sieve to effectively isolate the inward diffused H^+ from the abundant OH^- in bulk alkaline electrolyte to create an artificially proton-enriched environment near the Pt catalytic surface.**

By assuming the WD (alkaline Volmer) step to be the rate-limiting step of the HER at pH=14, the exchange current density corrected by the promoted WD kinetics can be estimated as an HER activity descriptor. The WD barriers on the outer surface or inside the NiO_xH_y are lower than on the bare Pt(111) by 0.43 or 0.73 eV, respectively. The accelerated WD kinetics, together with the proton-permeability of the NiO_xH_y matrix, boosts the effective proton supply to the Pt surface for the later Tafel step. The activity of the Pt@NiO_xH_y system is hence substantially increased from the $10^{-11.2}$ A/cm^2 of bare Pt(111) to the range of $10^{-6.1}$ to $10^{-1.1}$ A/cm^2 (mixed contribution from inner and outer WD sites in NiO_xH_y, respectively) (Fig. 4e), largely comparable to the performance of Pt(111) at pH=0 ($10^{-3.2}$ A/cm^2).

Although the WD kinetics of transition metal hydroxides have been suggested to explain the enhanced HER activity of Pt/transition metal oxide catalysts, a direct measurement of the enhanced WD steps on electrocatalyst is challenging due to the difficulties to decouple with subsequent hydrogen production steps. To directly elucidate the role of the amorphous $Ni(OH)_2$ shell as an efficient WD catalyst, we tested the WD activity of the $Ni(OH)_2$ shell by using bipolar membrane (BPM) electrolysis. The BPM electrolysis is conducted in an H-cell where a combination of AEM and PEM is used to separate the acidic HER half-cell (pH=0) and alkaline OER half-cell (pH=14). The Pt_{tet}@$Ni(OH)_2$ or Pt_{tet} were uniformly dispersed at the interface between the PEM and AEM as the WD catalysts. The standard potential required to drive WD is 0.83 V[50,51], above which the WD current increases exponentially until reaching the mass transport limit. The WD polarization curves (Extended Data Fig. 18) reveal that the pure BPM with no catalyst, with the naked Pt_{tet} core or with crysalline $Ni(OH)_2$ nanoplates require an overpotential of 1.64 V, 0.97 V, and 0.64 V, respectively, to reach the 50 mA/cm^2, while that with the amorphous $Ni(OH)_2$ shell (in Pt_{tet}@$Ni(OH)_2$) only needs 0.18 V overpotential to reach 50 mA/cm^2, demonstrating a much faster WD kinetics, and experimentally confirming the exceptional WD catalytic activity of the amorphous $Ni(OH)_2$.

Electrochemical HER performance of Pt_{tet}@$Ni(OH)_2$

With greatly improved HER kinetics from the selective enrichment of proton by the $Ni(OH)_2$ proton sieve, the Pt_{tet}@$Ni(OH)_2$ coreshell catalysts show a record-high specific activity (SA) of 27.7 mA/cm^2 Pt at -70 mV vs. RHE at pH 14, which is 28 times and 6 times that of Pt/C and naked Pt_{tet}, respectively; and considerably higher than the previous state-of-art (14.8 mA/cm^2 Pt@ -70 mV vs. RHE) (Fig. 5a).[3,4,43,46,47,52] We note the SA achieved with Pt_{tet}@$Ni(OH)_2$ is also higher than that of the recently reported Pt-shell catalysts with elaborate strain engineering on Pd nanocubes.[53] Further, since the $Ni(OH)_2$ shell only moderately reduces the ECSA, such a high SA observed in Pt_{tet}@$Ni(OH)_2$ has also directly led to a record-high MA of 13.4 A/mg$_{Pt}$ @ -70 mV vs. RHE, which is 18-fold higher than that of the commercial Pt/C, and 4.6-fold of that of naked Pt_{tet}; and represent the best among the state-of-the-art Pt-based HER catalysts in the alkaline electrolyte (Extended Data Table 6).[3,4,6,17,18,43,46,47,52,54] Additionally, considering the greatly reduced Tafel slope with the Pt_{tet}@$Ni(OH)_2$ design, the relative benefit of the increased SA and MA could be further amplified at higher overpotential in practical HER conditions.

The proton conductive $Ni(OH)_2$ shell could help isolate the active Pt sites from the bulk electrolyte environment and thus improve the catalytic tolerance to water impurities with competitive adsorption or capability of etching. For example, halide anions (e.g., Cl^-) represent common impurity anions that can strongly bind with Pt sites and partly suppress the catalytic activity. In this regard, the amorphous $Ni(OH)_2$ shell may help block halide anions from the active Pt sites due to the lack of transport path and Donnan exclusion effect.[55] To this end, we have evaluated the Cl^- and I^- tolerance of the Pt_{tet}@$Ni(OH)_2$ and the naked Pt_{tet} catalysts. Notably, the Pt_{tet}@$Ni(OH)_2$ maintains essentially the same HER current level in the presence of 0.5 M Cl^- or 0.25 M I^- in electrolyte, while the Pt_{tet} shows a substantial current drop by 26% and 52%, respectively (Fig. 5b and Extended Data Fig. 19). **Such a high tolerance to ionic impurities could help relax the water purity requirements in practical water electrolysis**, which is a largely unaddressed matter but could be significant since the cost of ultrapure water and the relevant circulation system constitutes a significant fraction (up to 13%) of the total hydrogen production cost.[56]

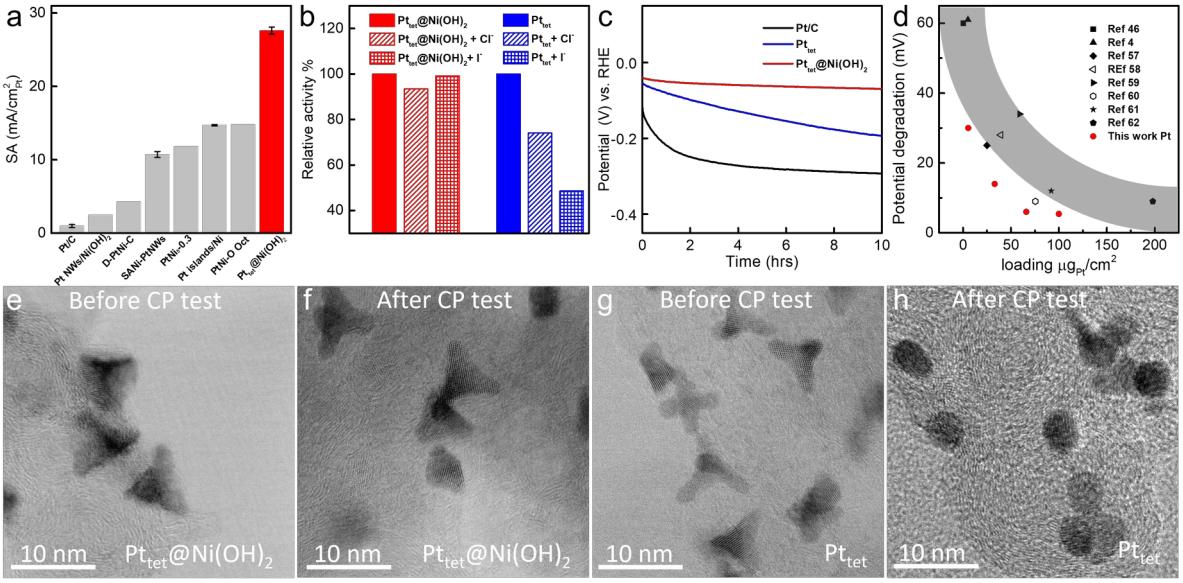

Figure 5| Evaluation of HER activity and stability a, Comparison of the specific activity (SA) of Pt_{tet}@$Ni(OH)_2$ with the state-of-the-art alkaline HER catalysts. Error bar is added unless they are not provided in the cited literature. **b,** Relative activity of Pt_{tet}@$Ni(OH)_2$ and Pt_{tet} in pure 1.0 M KOH, 1.0 M KOH + 0.5 M Cl^-, and 1.0 M KOH + 0.25 M I^-. **c,** Chronopotentiometry (CP) stability test of Pt_{tet}@$Ni(OH)_2$, $Pt_{tet,}$ and Pt/C. **d,** Comparison of the stability of Pt_{tet}@$Ni(OH)_2$ with different loading with the state-of-the-art alkaline HER catalysts. We should note that there are numerous parameters in the stability tests, including Pt loading amount, current density, operation time, etc. It is extremely difficult to have all the parameters identical when compared with the literature data. Here we

specifically selected the stability results from the literature which conduct the CP test with a fixed current density at 10 mA/cm^2 (Ref 59 is under 20 mA/cm^2) and duration longer than 10 hours. Only the potential degradation data within the first 10 hours are taken into consideration. (**e-h**) Representative HRTEM images of Pt_{tet}@$Ni(OH)_2$ and Pt_{tet} before and after the stability tests.

Additionally, the $Ni(OH)_2$ encapsulation can also prevent the Pt surface from dissolution, leaching, ripening, or aggregation. Chronopotentiometry (CP) tests were conducted to evaluate the durability of the Pt_{tet}@$Ni(OH)_2$ catalysts at a constant current of 10 mA/cm^2 (normalized by electrode geometrical area). Our CP studies show that Pt_{tet}@$Ni(OH)_2$ coreshell catalysts exhibit only a 30 mV overpotential increase over the 10-hour continuous test (Fig. 5c), much lower than those of naked Pt_{tet} and Pt/C under the same test conditions (140.5 mV and 177 mV potential degradation in 10 hours, respectively). We note that such CP test evaluation of HER catalyst durability is highly dependent on the catalyst loading amount. To more comprehensively compare the stability of our Pt_{tet}@$Ni(OH)_2$ catalysts with other Pt HER catalysts under similar operation conditions, we plotted the potential degradation vs. the loading amount of different catalysts reported in recent literature (Fig. 5d and Extended Data Fig. 20).[4,46,57-62] It is apparent that the potential degradation decreases substantially with the increasing Pt loading. This is not surprising since higher loading usually comes with more active surface sites, which reduces the average catalytic current per active site and thus reduces the chemical stress or slows the surface degradation process. Indeed, our Pt_{tet}@$Ni(OH)_2$ catalysts with 4 different loading amounts show a similar trend with a notably smaller potential degradation at the higher catalyst loading levels (Fig. 5d and Extended Data Fig. 20). More importantly, the potential degradation of Pt_{tet}@$Ni(OH)_2$ catalysts is considerably below the reference curve, demonstrating the more stable nature of the Pt_{tet}@$Ni(OH)_2$ coreshell catalysts (Fig. 5d).

In general, the Pt nanocatalysts typically feature a relatively high surface energy, and may readily undergo surface reconstruction or ripening process to minimize the total surface energy,[63] particularly under HER conditions where the dynamic interaction with surface bonded H atoms (Pt-H) was found to considerably accelate surface Pt atom diffusion[64]. Such surface reconstruction or ripening process could lead to the loss of originally designed surface structure and the irreversible activity degradation. In this regard, the encapsulating $Ni(OH)_2$ proton conductive shell in Pt_{tet}@$Ni(OH)_2$ can effectively retards Pt surface atom migration to ensure high structural stability and durable activity ~~durability~~. Indeed, our studies demonstrate that the

tetrahedral shape of Pt_{tet}@$Ni(OH)_2$ and the embedded Pt tetrapods are well-retained (Fig. 5e, f; and Extended Data Fig. 21) with little Pt loss after the long-term durability test. In contrast, the naked Pt_{tet} without $Ni(OH)_2$ shell undergoes severe ripening with higher Pt loss during the stability test and turns into nearly spherical nanoparticles (Fig. 5g, h and ; and Extended Data Fig. 22). Our additional statbility test with periodic surface cleaning reveal that the actvity loss observed in Pt_{tet}@$Ni(OH)_2$ can be largely recoved after surface cleaning, inicating little irreversible catalyst degradation, which is consistent with the well-retained coreshell morphology. On the other hand, the Pt_{tet} and Pt/C show considerable irreversible degradation due to the severe surface reconstruction and ripening behavior (Extended Data Fig. 22).

Conclusion

In summary, we have reported a unique design of "$Ni(OH)_2$-clothed Pt-tetrapod" coreshell nanostructure, in which the amorphous $Ni(OH)_2$ shell functions as a water dissociation catalyst and proton conductive shell to isolate the catalytic Pt surface from the bulk alkaline electrolyte while ensuring efficient proton supply to Pt sites. It delivers an acidic-like HER kinetics in bulk alkaline electrolyte, with the lowest Tafel slope and the highest alkaline HER activity among all Pt-based catalysts reported to date. Moreover, the encapsulation of the catalytic surface by the proton conductive shell considerably slows the dissolution/diffusion of Pt atoms from catalytic surfaces and suppresses the undesirable poisoning effect from impurity ions, thus ensuring high structural stability and activity durability that is difficult to achieve in the naked Pt-catalyst designs. The markedly improved alkaline HER activity and presents an attractive catalyst material for alkaline water electrolyzers and renewable chemical fuel generation. Additionally, the demonstrated capability to fundamentally modify the reaction kinetics by tailoring the local chemical environment may be expanded as a general strategy for the design of a new generation of electrocatalysts with a favorable reaction environment and high selectivity or durability for a wide range of fundamentally and technologically important electrochemical reactions.

References

1 **Cao, Z. *et al.* Platinum-nickel alloy excavated nano-multipods with hexagonal close-packed structure and superior activity towards hydrogen evolution reaction. *Nature Communications* 8, 15131, (2017).**

2 **Danilovic, N. *et al.* Enhancing the alkaline hydrogen evolution reaction activity through the bifunctionality of Ni (OH) 2/metal catalysts. *Angewandte Chemie* 124, 12663-12666, (2012).**

3 Yin, H. *et al.* Ultrathin platinum nanowires grown on single-layered nickel hydroxide with high hydrogen evolution activity. *Nature communications* 6, 6430, (2015).
4 Zhao, Z. *et al.* Surface-engineered PtNi-O nanostructure with record-high performance for electrocatalytic hydrogen evolution reaction. *Journal of the American Chemical Society* 140, 9046-9050, (2018).
5 Subbaraman, R. *et al.* Trends in activity for the water electrolyser reactions on 3d M (Ni, Co, Fe, Mn) hydr (oxy) oxide catalysts. *Nature materials* 11, 550, (2012).
6 Liu, Z. *et al.* Aqueous Synthesis of Ultrathin Platinum/Non-Noble Metal Alloy Nanowires for Enhanced Hydrogen Evolution Activity. *Angewandte Chemie* 130, 11852-11856, (2018).
7 Reier, T., Nong, H. N., Teschner, D., Schlögl, R. & Strasser, P. Electrocatalytic Oxygen Evolution Reaction in Acidic Environments – Reaction Mechanisms and Catalysts. *Advanced Energy Materials* 7, 1601275, (2017).
8 Suen, N.-T. *et al.* Electrocatalysis for the oxygen evolution reaction: recent development and future perspectives. *Chemical Society Reviews* 46, 337-365, (2017).
9 Schalenbach, M. *et al.* Acidic or Alkaline? Towards a New Perspective on the Efficiency of Water Electrolysis. *Journal of The Electrochemical Society* 163, F3197-F3208, (2016).
10 Leng, Y. *et al.* Solid-State Water Electrolysis with an Alkaline Membrane. *Journal of the American Chemical Society* 134, 9054-9057, (2012).
11 Abbasi, R. *et al.* A Roadmap to Low-Cost Hydrogen with Hydroxide Exchange Membrane Electrolyzers. *Advanced Materials* 0, 1805876, (2019).
12 Tian, X., Zhao, P. & Sheng, W. Hydrogen Evolution and Oxidation: Mechanistic Studies and Material Advances. *Advanced Materials* 31, 1808066, (2019).
13 Energy, U. S. D. o. Hydrogen and Fuel Cells Program: 2019 Annual Merit Review and Peer Evaluation Report. (2019).
14 Zeng, K. & Zhang, D. Recent progress in alkaline water electrolysis for hydrogen production and applications. *Progress in Energy and Combustion Science* 36, 307-326, (2010).
15 Cao, L. *et al.* Atomically dispersed iron hydroxide anchored on Pt for preferential oxidation of CO in H2. *Nature* 565, 631-635, (2019).
16 Shen, K., Chen, X., Chen, J. & Li, Y. Development of MOF-Derived Carbon-Based Nanomaterials for Efficient Catalysis. *ACS Catalysis* 6, 5887-5903, (2016).
17 Wang, P. *et al.* Precise tuning in platinum-nickel/nickel sulfide interface nanowires for synergistic hydrogen evolution catalysis. *Nature Communications* 8, 14580, (2017).
18 Wang, P., Jiang, K., Wang, G., Yao, J. & Huang, X. Phase and Interface Engineering of Platinum–Nickel Nanowires for Efficient Electrochemical Hydrogen Evolution. *Angewandte Chemie International Edition* 55, 12859-12863, (2016).
19 Elbaz, Y., Furman, D. & Caspary Toroker, M. Hydrogen transfer through different crystal phases of nickel oxy/hydroxide. *Physical Chemistry Chemical Physics* 20, 25169-25178, (2018).
20 Beatty, M. E. S., Chen, H., Labrador, N. Y., Lee, B. J. & Esposito, D. V. Structure–property relationships describing the buried interface between silicon oxide

overlayers and electrocatalytic platinum thin films. *Journal of Materials Chemistry A* 6, 22287-22300, (2018).

21 Sun, B., Snaith, H. J., Dhoot, A. S., Westenhoff, S. & Greenham, N. C. Vertically segregated hybrid blends for photovoltaic devices with improved efficiency. *Journal of Applied Physics* 97, 014914, (2005).

22 Li, H. B. *et al.* Amorphous nickel hydroxide nanospheres with ultrahigh capacitance and energy density as electrochemical pseudocapacitor materials. *Nature Communications* 4, 1894, (2013).

23 Huang, W. *et al.* Highly active and durable methanol oxidation electrocatalyst based on the synergy of platinum–nickel hydroxide–graphene. *Nature Communications* 6, 10035, (2015).

24 Payne, B. P., Biesinger, M. C. & McIntyre, N. S. The study of polycrystalline nickel metal oxidation by water vapour. *Journal of Electron Spectroscopy and Related Phenomena* 175, 55-65, (2009).

25 Mansour, A. N. Characterization of β-Ni(OH)2 by XPS. *Surface Science Spectra* 3, 239-246, (1994).

26 Peck, M. A. & Langell, M. A. Comparison of Nanoscaled and Bulk NiO Structural and Environmental Characteristics by XRD, XAFS, and XPS. *Chemistry of Materials* 24, 4483-4490, (2012).

27 Mathew, K., Sundararaman, R., Letchworth-Weaver, K., Arias, T. A. & Hennig, R. G. Implicit solvation model for density-functional study of nanocrystal surfaces and reaction pathways. *The Journal of Chemical Physics* 140, 084106, (2014).

28 Rebollar, L. *et al.* "Beyond Adsorption" Descriptors in Hydrogen Electrocatalysis. *ACS Catalysis* 10, 14747-14762, (2020).

29 Nai, J., Wang, S., Bai, Y. & Guo, L. Amorphous Ni(OH)2 Nanoboxes: Fast Fabrication and Enhanced Sensing for Glucose. *Small* 9, 3147-3152, (2013).

30 Gan, L. *et al.* Element-specific anisotropic growth of shaped platinum alloy nanocrystals. *Science* 346, 1502-1506, (2014).

31 Sheng, W. *et al.* Correlating hydrogen oxidation and evolution activity on platinum at different pH with measured hydrogen binding energy. *Nature Communications* 6, 5848, (2015).

32 Wang, X., Xu, C., Jaroniec, M., Zheng, Y. & Qiao, S.-Z. Anomalous hydrogen evolution behavior in high-pH environment induced by locally generated hydronium ions. *Nature Communications* 10, 4876, (2019).

33 Podjaski, F. *et al.* Rational strain engineering in delafossite oxides for highly efficient hydrogen evolution catalysis in acidic media. *Nature Catalysis* 3, 55-63, (2020).

34 Fang, S. *et al.* Uncovering near-free platinum single-atom dynamics during electrochemical hydrogen evolution reaction. *Nature Communications* 11, 1029, (2020).

35 Li, F. *et al.* Balancing hydrogen adsorption/desorption by orbital modulation for efficient hydrogen evolution catalysis. *Nature Communications* 10, 4060, (2019).

36 Liang, L. *et al.* Cobalt single atom site isolated Pt nanoparticles for efficient ORR and HER in acid media. *Nano Energy* 88, 106221, (2021).

37 Zheng, J., Yan, Y. & Xu, B. Correcting the Hydrogen Diffusion Limitation in Rotating Disk Electrode Measurements of Hydrogen Evolution Reaction Kinetics. *Journal of The Electrochemical Society* 162, F1470-F1481, (2015).
38 Rheinländer, P. J., Herranz, J., Durst, J. & Gasteiger, H. A. Kinetics of the Hydrogen Oxidation/Evolution Reaction on Polycrystalline Platinum in Alkaline Electrolyte Reaction Order with Respect to Hydrogen Pressure. *Journal of The Electrochemical Society* 161, F1448-F1457, (2014).
39 Markovića, N. M., Sarraf, S. T., Gasteiger, H. A. & Ross, P. N. Hydrogen electrochemistry on platinum low-index single-crystal surfaces in alkaline solution. *Journal of the Chemical Society, Faraday Transactions* 92, 3719-3725, (1996).
40 Marković, N. M., Grgur, B. N. & Ross, P. N. Temperature-Dependent Hydrogen Electrochemistry on Platinum Low-Index Single-Crystal Surfaces in Acid Solutions. *The Journal of Physical Chemistry B* 101, 5405-5413, (1997).
41 Shinagawa, T., Garcia-Esparza, A. T. & Takanabe, K. Insight on Tafel slopes from a microkinetic analysis of aqueous electrocatalysis for energy conversion. *Scientific Reports* 5, 13801, (2015).
42 Zheng, Y., Jiao, Y., Vasileff, A. & Qiao, S.-Z. The Hydrogen Evolution Reaction in Alkaline Solution: From Theory, Single Crystal Models, to Practical Electrocatalysts. *Angewandte Chemie International Edition* 57, 7568-7579, (2018).
43 Li, M. *et al.* Single-atom tailoring of platinum nanocatalysts for high-performance multifunctional electrocatalysis. *Nature Catalysis* 2, 495-503, (2019).
44 Wang, Y., Chen, L., Yu, X., Wang, Y. & Zheng, G. Superb Alkaline Hydrogen Evolution and Simultaneous Electricity Generation by Pt-Decorated Ni3N Nanosheets. *Advanced Energy Materials* 7, 1601390, (2017).
45 Jiang, Y. *et al.* Coupling PtNi Ultrathin Nanowires with MXenes for Boosting Electrocatalytic Hydrogen Evolution in Both Acidic and Alkaline Solutions. *Small* 15, 1805474, (2019).
46 Alinezhad, A. *et al.* Direct Growth of Highly Strained Pt Islands on Branched Ni Nanoparticles for Improved Hydrogen Evolution Reaction Activity. *Journal of the American Chemical Society* 141, 16202-16207, (2019).
47 Chen, H. *et al.* Effect of Atomic Ordering Transformation of PtNi Nanoparticles on Alkaline Hydrogen Evolution: Unexpected Superior Activity of the Disordered Phase. *The Journal of Physical Chemistry C* 124, 5036-5045, (2020).
48 Wang, G., Huang, X., Liao, H.-G. & Sun, S.-G. Microstrain Engineered NixS2/PtNi Porous Nanowires for Boosting Hydrogen Evolution Activity. *Energy & Fuels* 35, 6928-6934, (2021).
49 Laasonen, K. & Klein, M. L. Structural Study of (H2O)20 and (H2O)21H+ Using Density Functional Methods. *The Journal of Physical Chemistry* 98, 10079-10083, (1994).
50 Oener, S. Z., Foster, M. J. & Boettcher, S. W. Accelerating water dissociation in bipolar membranes and for electrocatalysis. *Science* 369, 1099-1103, (2020).
51 Tufa, R. A. *et al.* Bipolar Membrane and Interface Materials for Electrochemical Energy Systems. *ACS Applied Energy Materials* 4, 7419-7439, (2021).

52 Zhang, C. *et al.* H2 In Situ Inducing Strategy on Pt Surface Segregation Over Low Pt Doped PtNi5 Nanoalloy with Superhigh Alkaline HER Activity. *Advanced Functional Materials* 31, 2008298, (2021).
53 He, T. *et al.* Mastering the surface strain of platinum catalysts for efficient electrocatalysis. *Nature* 598, 76-81, (2021).
54 Zhou, K. L. *et al.* Platinum single-atom catalyst coupled with transition metal/metal oxide heterostructure for accelerating alkaline hydrogen evolution reaction. *Nature Communications* 12, 3783, (2021).
55 Sarkar, S., SenGupta, A. K. & Prakash, P. The Donnan Membrane Principle: Opportunities for Sustainable Engineered Processes and Materials. *Environmental Science & Technology* 44, 1161-1166, (2010).
56 Mayyas, A. T., Ruth, M. F., Pivovar, B. S., Bender, G. & Wipke, K. B. Manufacturing Cost Analysis for Proton Exchange Membrane Water Electrolyzers. Medium: ED; Size: 3.3 MB (United States, 2019).
57 Zhang, H. *et al.* Open hollow Co–Pt clusters embedded in carbon nanoflake arrays for highly efficient alkaline water splitting. *Journal of Materials Chemistry A* 6, 20214-20223, (2018).
58 Xing, Z., Han, C., Wang, D., Li, Q. & Yang, X. Ultrafine Pt Nanoparticle-Decorated Co(OH)2 Nanosheet Arrays with Enhanced Catalytic Activity toward Hydrogen Evolution. *ACS Catalysis* 7, 7131-7135, (2017).
59 Song, H. J., Sung, M.-C., Yoon, H., Ju, B. & Kim, D.-W. Ultrafine α-Phase Molybdenum Carbide Decorated with Platinum Nanoparticles for Efficient Hydrogen Production in Acidic and Alkaline Media. *Advanced Science* 6, 1802135, (2019).
60 Xie, L. *et al.* A Ni(OH)2–PtO2 hybrid nanosheet array with ultralow Pt loading toward efficient and durable alkaline hydrogen evolution. *Journal of Materials Chemistry A* 6, 1967-1970, (2018).
61 Zhao, W. *et al.* Key Single-Atom Electrocatalysis in Metal—Organic Framework (MOF)-Derived Bifunctional Catalysts. *ChemSusChem* 11, 3473-3479, (2018).
62 Jang, S. W. *et al.* Holey Pt Nanosheets on NiFe-Hydroxide Laminates: Synergistically Enhanced Electrocatalytic 2D Interface toward Hydrogen Evolution Reaction. *ACS Nano* 14, 10578-10588, (2020).
63 McCrum, I. T., Hickner, M. A. & Janik, M. J. First-Principles Calculation of Pt Surface Energies in an Electrochemical Environment: Thermodynamic Driving Forces for Surface Faceting and Nanoparticle Reconstruction. *Langmuir* 33, 7043-7052, (2017).
64 Horch, S. *et al.* Enhancement of surface self-diffusion of platinum atoms by adsorbed hydrogen. *Nature* 398, 134-136, (1999).
65 Ravel, B. & Newville, M. ATHENA, ARTEMIS, HEPHAESTUS: data analysis for X-ray absorption spectroscopy using IFEFFIT. *Journal of Synchrotron Radiation* 12, 537-541, (2005).
66 Rehr, J. J. & Albers, R. C. Theoretical approaches to x-ray absorption fine structure. *Reviews of Modern Physics* 72, 621-654, (2000).
67 Alexandrova, A. N. & Boldyrev, A. I. Search for the Lin0/+1/-1 (n = 5–7) Lowest-Energy Structures Using the ab Initio Gradient Embedded Genetic Algorithm

(GEGA). Elucidation of the Chemical Bonding in the Lithium Clusters. *Journal of Chemical Theory and Computation* 1, 566-580, (2005).

68 Vilhelmsen, L. B. & Hammer, B. A genetic algorithm for first principles global structure optimization of supported nano structures. *The Journal of Chemical Physics* 141, 044711, (2014).

69 Zhang, Z. & Wang, Y.-G. Molecular Design of Dispersed Nickel Phthalocyanine@Nanocarbon Hybrid Catalyst for Active and Stable Electroreduction of CO2. *The Journal of Physical Chemistry C* 125, 13836-13849, (2021).

70 Sun, G., Alexandrova, A. N. & Sautet, P. Pt8 cluster on alumina under a pressure of hydrogen: Support-dependent reconstruction from first-principles global optimization. *The Journal of Chemical Physics* 151, 194703, (2019).

71 Wexler, R. B., Qiu, T. & Rappe, A. M. Automatic Prediction of Surface Phase Diagrams Using Ab Initio Grand Canonical Monte Carlo. *The Journal of Physical Chemistry C* 123, 2321-2328, (2019).

72 Tipton, W. W. & Hennig, R. G. A grand canonical genetic algorithm for the prediction of multi-component phase diagrams and testing of empirical potentials. *Journal of Physics: Condensed Matter* 25, 495401, (2013).

73 Zhai, H. & Alexandrova, A. N. Ensemble-Average Representation of Pt Clusters in Conditions of Catalysis Accessed through GPU Accelerated Deep Neural Network Fitting Global Optimization. *Journal of Chemical Theory and Computation* 12, 6213-6226, (2016).

74 Deaven, D. M. & Ho, K. M. Molecular Geometry Optimization with a Genetic Algorithm. *Physical Review Letters* 75, 288-291, (1995).

75 Adamo, C. & Barone, V. Toward reliable density functional methods without adjustable parameters: The PBE0 model. *The Journal of Chemical Physics* 110, 6158-6170, (1999).

76 Kresse, G. & Joubert, D. From ultrasoft pseudopotentials to the projector augmented-wave method. *Physical Review B* 59, 1758-1775, (1999).

77 Kresse, G. & Furthmüller, J. Efficient iterative schemes for ab initio total-energy calculations using a plane-wave basis set. *Physical Review B* 54, 11169-11186, (1996).

78 Kresse, G. & Furthmüller, J. Efficiency of ab-initio total energy calculations for metals and semiconductors using a plane-wave basis set. *Computational Materials Science* 6, 15-50, (1996).

79 Kresse, G. & Hafner, J. Ab initio molecular dynamics for liquid metals. *Physical Review B* 47, 558-561, (1993).

80 Kresse, G. & Hafner, J. Ab initio molecular-dynamics simulation of the liquid-metal--amorphous-semiconductor transition in germanium. *Physical Review B* 49, 14251-14269, (1994).

81 Grimme, S., Antony, J., Ehrlich, S. & Krieg, H. A consistent and accurate ab initio parametrization of density functional dispersion correction (DFT-D) for the 94 elements H-Pu. *The Journal of Chemical Physics* 132, 154104, (2010).

82 Mathew, K., Kolluru, V. S. C., Mula, S., Steinmann, S. N. & Hennig, R. G. Implicit self-consistent electrolyte model in plane-wave density-functional theory. *The Journal of Chemical Physics* 151, 234101, (2019).

83 **Yu, M. & Trinkle, D. R. Accurate and efficient algorithm for Bader charge integration.** ***The Journal of Chemical Physics*** **134, 064111, (2011).**
84 **Nørskov, J. K.** ***et al.*** **Trends in the Exchange Current for Hydrogen Evolution.** ***Journal of The Electrochemical Society*** **152, J23, (2005).**
85 **Nørskov, J. K.** ***et al.*** **Origin of the Overpotential for Oxygen Reduction at a Fuel-Cell Cathode.** *The Journal of Physical Chemistry B* **108**, 17886-17892, (2004).

Methods

Chemicals. Platinum(II) acetylacetonate [$Pt(acac)_2$, Pt 48.0%], nickel(II) acetylacetonate [$Ni(acac)_2$, 95%], glucose, tungsten(0) hexacarbonyl ($W(CO)_6$, 97%), oleylamine (> 98%), 1-octadecene (ODE, > 90%), nickel(II) nitrate hexahydrate [$Ni(NO_3)_2{\cdot}6H_2O$], Cetrimonium bromide ($[(C_{16}H_{33})N(CH_3)_3]Br$ and Nafion® 117 solution (~ 5%) were purchased from Sigma Aldrich. Commercial Pt/C catalyst (10 wt% Pt, and particle size ~ 2 nm) was purchased from Alfa Aesar. Ethanol (200 proof) was obtained from Decon Labs, Inc. Potassium hydroxide (KOH) was purchased from Fisher Chemical. All the above reagents were used as received without further purification. Carbon black (Vulcan XC-72) was received from Cabot Corporation and was annealed for 2 hours under Ar gas environment at 400 ℃ before being used. The deionized water (18 MΩ/cm) was obtained from an ultra-pure purification system (Milli-Q advantage A10). The Naftion™ 117 (PEM) and the Fumasep Fas-50 (AEM) were purchased from the Fuel cell Store.

Synthesis. In a 30 mL glass vial, 20 mg $Pt(acac)_2$, 25.6 mg $Ni(acac)_2$, 32 mg $W(CO)_6$ and 135 mg glucose were dissolved in a mixture of 3 mL oleylamine and 2 mL octadecene. The mixture was sonicated for 1 hour and the resulting homogenous solution was kept at 80 °C for 2.5 hours and then heated to 140 °C for another 8 hours. After the reaction, the precipitate was centrifuged out at 12100 r.p.m. and washed by ethanol/hexane (25 mL/5 mL) three times. The final product was suspended in 10 mL cyclohexane. In a 30 mL glass vial, 30 mg carbon black (the carbon black was annealed under Ar at 200 °C for 1 hour before use) was sonicated in 15 mL ethanol for 1 hour. 5 mL Pt_{tet}@$Ni(OH)_2$ hexane solution was then added into the carbon black/ethanol solution and the mixture was sonicated for another 1 hour. The catalysts were centrifuged out at 12100 r.p.m. and washed with cyclohexane/ethanol solution three times, followed by being dried in the vacuum oven for 1 hour. The Pt_{tet}@$Ni(OH)_2$/C were then annealed in the air at 200 °C for 2 hours to fully remove the surface remaining ligands. The Pt yield is about 40%, on the scale of 6 mg_{Pt}/ batch. It has been scaled up to 120 mg_{Pt} per batch. The crystalline $Ni(OH)_2$ nanoplates

were synthesized via adding 0.5 mL 30 wt% ammonia water drop by drop into 100 mL $Ni(NO)_3$ solution (10g/L) with 0.25 g CTAB as the surfactant.

Characterizations. Transmission electron microscopy (TEM) images were taken on an FEI T12 operated at 120 kV. Atomic resolution high angle annular dark-field scanning transmission electron microscopy (HAADF-STEM) images and X-ray energy dispersive spectroscopy (EDS) mapping were taken on FEI Titan Cubed Themis G2 300 at 200 kV and JEOL Grand ARM 300CF TEM/STEM with double spherical aberration-correctors operated at 300 kV. Samples for TEM measurements were prepared by dropping 10-20 μL nanoparticles dispersion in hexane on a carbon-coated copper grid (Ladd Research, Williston, VT). Powder X-ray diffraction patterns (PXRD) were collected on a Panalytical X'Pert Pro X-ray Powder Diffractometer with Cu-Kα radiation. The composition of catalysts was determined by inductively coupled plasma atomic emission spectroscopy (ICP- AES, Shimadzu ICPE-9000) as well as SEM-EDS (JEOL JSM-6700F FE-SEM). X-ray photoelectron spectroscopy (XPS) tests were done with Kratos AXIS Ultra DLD spectrometer.

X-ray adsorption data analysis. Ni K-edge and Pt L_3-edge X-ray absorption spectra were acquired under ambient conditions in fluorescence and transmission modes at beamline 1W2B of the Beijing Synchrotron Radiation Facility(BSRF), using a Si (111) double-crystal monochromator. The storage ring of BSRF was operated at 2.5 GeV with a maximum current of 250 mA in top-up mode. While the energy was calibrated using Ni/Pt foil, the incident, transmitted and fluorescent X-ray intensities were monitored by using standard ion chambers and Lytle-type detector, respectively.

XAS analysis was performed according to standard procedures using the ATHENA and ARTEMIS modules implemented in the IFEFFIT software package.[65] The EXAFS signal was first obtained by background-subtraction and normalization, then the χ(k) data were Fourier-transformed to real (R) space using a Hanning window. To obtain the quantitative structural parameters around the central atoms, a least-squares curve-fitting analysis of the EXAFS χ(k) data was carried out based on the EXAFS equation in R-space. The structural models were constructed based on the crystal structures of $Ni(OH)_2$, with the scattering amplitudes, phase shifts, and photoelectron mean free path for all paths calculated with the ab initio code FEFF 8.5.[66]

Electrochemical Measurements. To obtain a homogeneous catalyst ink, 1 mg of dried Pt_{tet}@$Ni(OH)_2$/C was mixed with 1 mL ethanol and sonicated for 5 minutes. Then, 10 μL (20 μL for stability test) of Nafion (5 wt%) was added to the solution. After sonication, 20 μL of the homogeneous ink was dropped onto a 5 mm diameter glassy carbon electrode (0.196 cm^2, Pine Research Instrumentation). The ink was dried under ambient air before electrochemical testing.

All electrochemical tests were carried out in a three-electrode cell from Pine Research Instrumentation. The working electrode was a glassy carbon rotating disk electrode (RDE) coated with corresponding catalysts. The reference electrode was a Hg/HgO electrode from CH Instrument and was calibrated in 1.0 M KOH with saturated H_2. A graphite rod was used as the counter electrode. Cyclic voltammetry was conducted in 1.0 M KOH and 1.0 M $HClO_4$ between 50 mV to 1100 mV vs. RHE at a sweep rate of 100 mV/s. The polarization curves were tested between -200 mV to 100 mV vs. RHE at a sweep rate of 5 mV/s in 1.0 M KOH and 1.0 M $HClO_4$ with a Pt loading of 5.1 μg/cm^2 for Pt/C and 5.6 μg/cm^2 for Pt_{tet}@$Ni(OH)_2$ and Pt_{tet}, under a rotation speed of 1600 r.p.m. The solution resistances were measured via impedance test. ECSA was measured through the hydrogen desorption region in N_2 saturated 1 M KOH. The bipolar membrane test was conducted in the H-cell. The BPM was fabricated by wet pressing the Nafion 117 PEM and the Fumasep Fas-30 AEM and removing all the bubbles in between two films. When desired, the WD catalysts were pre-deposited on the PEM and the press together with AEM to form BPM with sandwiched WD-CL. The stability test was performed with chronopotentiometry under 10 mA/cm^2 in Ar purged KOH for 10 hours.

Computational Methods: GCGA sampling. To sample the non-stoichiometric chemical subspace efficiently, we use the grand canonical genetic algorithm (GCGA) as implemented in our open-source Python package GOCIA (https://github.com/zishengz/gocia). The GA is an evolutionary global optimization algorithm that has been successfully applied to various fields including molecular design and structural search of gas-phase and supported clusters,[67-69] and the GC feature in our program allows variation of both the compositional and geometrical degrees of freedom to explore a larger chemical space of surface restructuring and adsorbates interactions, with minimal prior knowledge.[70,71] GCGA has been employed to efficiently explore the non-stoichiometric restructuring, under a certain chemical potential, of trinary alloys, 2D materials, supported metal clusters, etc.[70,72]

In the GCGA algorithm, the grand canonical free energy (grand potential) instead of the potential energy is the quantity to optimize. The grand potential is approximated by:

$$\Delta G = E(slab) - E(substrate) - \sum N_i \mu_i \quad (1)$$

Where $E(slab)$ is the electronic energy of the whole optimized slab; $E(substrate)$ is the electronic energy of the Pt(111) substrate; N_i is the number of element *i* atoms in the adlayer; μ_i is the chemical potential of element *i* which are estimated from reference species as follows:

$$\mu_{¿} = E¿ \quad (2)$$

$$\mu_H = \frac{1}{2} E(H_2) + 2.3 k_B T\, pH \quad (3)$$

$$\mu_O = E(H_2O) - 2\mu_H \quad (4)$$

A population size of 30 and a mutation rate of 30% are chosen for the GCGA sampling. The pool of initial candidates is generated using the bond length distribution algorithm (BLDA) which is a random structure generation method based on the covalent radii of the atoms.[73] A pre-optimization with Hookean potential is performed to produce reasonable starting geometries before they are fed to electronic structure method codes for local optimization and energy evaluation. Mating between the candidates alive to create offspring by the Split-and-splice operation,[74] in which the parent slabs are cut along a random plane and then spliced together. The fitness factor is assigned to each candidate based on the mating counts and the grand canonical free energy. Candidates with higher fitness are more probable to mate. The similarity check against the current population is performed before adding any new candidate to remove duplicates. Mutation of the randomly chosen offspring by adding or removing an adatom or adsorbate, or by rattling the surface atoms along random vectors drawn from a normal distribution. If an offspring is too similar to its parent, its mutation rate is raised to 100%. Upon the addition of each offspring to the population, the candidate with the lowest fitness is archived to maintain the population size. The structures with detached NiO_xH_y layers or unbound water molecules are removed from the population to avoid sampling into chemically irrelevant regions of the PES. A flowchart summarizing the workflow of the automated GCGA sampling is provided in Extended Data Fig. 11.

Note that the ratio of exposed surface Pt atoms (1/16 for the GM structure) may be underestimated due to sampling constraints as described in the last paragraph to focus the GCGA search direction on the interfacial structures. However, this model could well reflect (1) the interfacial structure where the Pt core and NiO_xH_y shell make the most contact and (2) the reactivity of NiO_xH_y and the hydrogen bond matrix that is still present even above the surface Pt regions that are less directly bonded to the NiO_xH_y layer.

Model set-up and DFT methods. The Pt surface is modeled by a 4-layer 4x4 supercell of Pt(111) surface termination with the upper two layers relaxed as a surface region while the bottom two layers are constrained as bulk region (Extended Data Fig. 11). A vacuum of 15 Å thickness is added in the Z direction to avoid spurious interactions between periodic images. The coverage of Ni was chosen to be 12 atoms per supercell for the production run, according to the lattice parameters of Pt (2.812 Å) and $Ni(OH)_2$ (3.165 Å):

$$16\,atoms/supercell \times \left(\frac{2.812\,\text{Å}}{3.165\,\text{Å}}\right)^2 \approx 12\,atoms/supercell \quad (5)$$

Which is the estimated minimal Ni coverage to fully cover the Pt(111) at the direct interface and to capture the interfacial chemistries while not heavy sample into the $Ni(OH)_2$-like regions.

The local optimization and energy evaluation of the generated structures are performed with the PBE functional[75] and PAW pseudopotentials[76] using the VASP program.[77-80] D3 correction is used to account for the dispersion interactions,[81] and dipole corrections are applied to remove the artificial electrostatic fields arising from asymmetric slabs in periodic boundary conditions. The convergence criteria for geometry (SCF) are set to 10^{-5} (10^{-6}) eV and 10^{-2} eV/Å for forces. Due to the relatively large system and sampling size, only the Γ *k*-point is sampled in the reciprocal space of the Brillouin zone throughout, and the cutoff energy for the kinetic energy of the plane-waves was 400 eV. Reaction energies are refined at higher cutoff energy of 500 eV and with the implicit solvation model using the VASPsol code.[27,82] The Bader charges are calculated from the charge density output using the Bader Charge Analysis code.[83]

Calculation of adsorption free energy and activation barriers.

The adsorption energy is calculated by:

$$\Delta E_H = E(¿H) - E(¿) - E(H) \quad (6)$$

where the * stands for the adsorption site. The adsorption free energy of H is calculated by:

$$\Delta G_H^o = \Delta E_H + ZPE(¿H) - T\Delta S_H \quad (7)$$

where the $(ZPE - T\Delta S_H)$ term at room temperature is taken from literature to be +0.24 eV [84]. The term is pH-independent and reflects the intrinsic adsorption property of the site at standard condition.

The pH-corrected adsorption free energy of H is calculated by shifting the chemical potential of the reference state of proton by the concentration dependence of the entropy, $-k_B T \ln[H^+] = \ln 10\, k_B T \mathrm{pH}$,[85] which yields:

$$\Delta G_H = \Delta G_H^o + \ln(10) k_B T\, pH \quad (8)$$

The exchange current densities i_0 are calculated from ΔG_H following the procedures described in Ref [84]. The preexponential factors are treated as the same for all the elementary steps.

Since the rate-limitng step of alkaline HER is the Volmer step, the kinetics of water dissociation is expected to induce a direct boost on the overall HER rate by controlling the rate of proton supply. Such thermochemistry-independent contribution is approximated by:

$$i' = \exp\left(\frac{-\Delta G_1^{\ddagger} - \Delta G_0^{\ddagger}}{k_B T}\right) \cdot i_0 \quad (9)$$

Where $\Delta G_0^{\ddagger}$ and $\Delta G_1^{\ddagger}$ represents the free enegry barrier of the water dissociation process on the reference system Pt(111) and other sites of interest in the restructured slab. The i' is the corrected exchange current density. The estimation assumes (i) that water dissociation on different sites shares the same preexponential factor; (ii) the HER rate is solely determined by the kinetics of the Volmer step, and the produced *H are consumed by Tafel step at Pt surface within a much shorter time scale; (iii) there are no significant recombination of proton and hydroxide from water dissociation because the hydrogen permeable NiOxHy effectively seperates the H^+ from the recombination with the OH^-.

Data availability

The data that support the plots within this paper and other findings of this study are available from the corresponding author upon reasonable request.

Acknowledgments. X.D. acknowledges support from the National Science Foundation award 1800580. Y.H. acknowledges support from the Office of Naval Research by the grant number N000141812155. A.N.A. acknowledges support by DOE-BES grant DE-SC0019152. X.P. acknowledges the support from the National Science Foundation award DMR-1506535. J.D. acknowledges financial support from the Youth Innovation Promotion Association of the Chinese Academy of Sciences (2018017). HAADF imaging and EDS mapping were carried out using the JEOL Grand ARM in the Irvine Materials Research Institute at the University of California, Irvine. J.D. and T.H. acknowledge the support from Beijing Synchrotron Radiation Facility. A.N.A. acknowledges the computational and storage resources from the National Energy Research Scientific Computing Center (NERSC), a U.S. Department of Energy Office of Science User Facility operated under Contract No. DE-AC02-05CH11231.

Author contributions. X.D. and Y.H. designed the research. C.W. performed the synthesis, most of the structural characterizations, and electrochemical tests. J.D. and T.H. performed the XAS measurement and analyzed the EXAFS and XANES data. Z.Z. and A.N.A. conducted DFT calculations. S.W., H.P., J.H., A.H.S. assisted in the synthesis. Z.L. and B.D. assisted in the SEM-EDS and XRD analysis. M.X conducted the aberration-corrected STEM characterization under the supervision of X.P. The paper was co-written by C.W., X.D., J.D., Z.Z., A.N.A. and Y.H. The research was supervised by X.D., Y.H. and A.N.A. All authors discussed the results and commented on the manuscript. **Competing interests:** The authors declare that they have no competing interests.

Competing financial interests. The authors declare no competing financial interests.

Additional information

Extended data is available for this paper.

Extended data

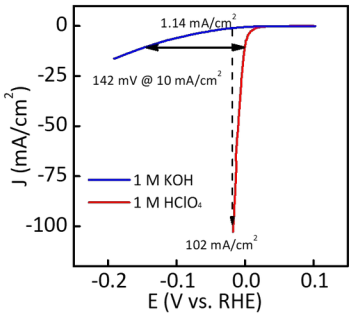

Extended Data Fig. 1| The comparison of Pt/C HER activity in acid and base. There is a 142 mV difference between the activity of Pt/C (5.1 $\mu g_{Pt}/cm^2$) in acid and base at a current density of 10 mA/cm^2. In a real application, the current is always on the scale of 500 mA/cm^2-1000 mA/cm^2, and the Tafel slopes in the acidic case and basic case are 29.6 mV/dec and 118.4 mV/dec respectively. Thus this potential difference will be significantly amplified at higher current density in the real application. Moreover, at -20 mV vs. RHE, the activity under pH 0 is about 89.5 times higher than that under pH 14, almost two orders of magnitude. For the same reason, the activity difference will also be amplified in the real application and will potentially be enlarged to 2-3 orders of magnitude, or even bigger.

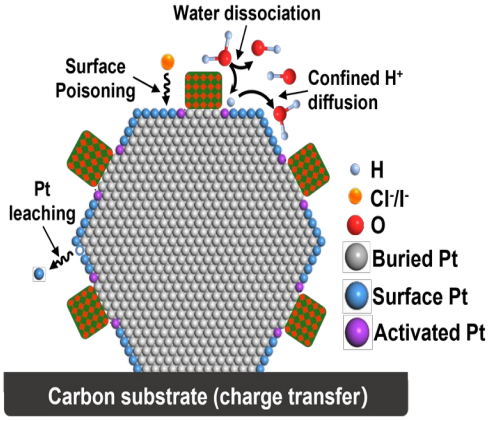

Extended Data Fig. 2| Pt NPs decorated with crystalline Ni species. The decoration of Pt surface with crystalline NiO_x or NiS_x species can partly facilitate water dissociation and activate nearby Pt for improved HER activity, but with two potential limitations that could compromise the overall activity: (i) Pt atoms buried under the crystalline NiO_x are not accessible to the electrolyte and hence cannot participate in the surface reaction; (ii) only the Pt sites in close proximity to the Ni sites can benefit from the enhanced water dissociation kinetics. The diffusion length of the generated H^+ is estimated to be ~1 nm in the alkaline electrolyte and cannot benefit Pt sites farther away from the Ni species can further migrate on the Pt surface to neighboring Pt sites, the adsorbed H will be comsumed immedaitely once being adsorbed due to the much faster Tafel step than the Volmer step during HER, and thus has a low possibility to spill over. Therefore despite partly enhanced kinetics, the majority of Pt sites are exposed to alkaline electrolyte and the HER and follow a typical Volmer- or Heyrovsky-step limited pathway with Tafel slopes of 40 mV/dec or larger. Moreover, the exposed Pt surface sites will undergo severe Oswald ripening during HER and gradually lose the designed nanostructure and the original activity.

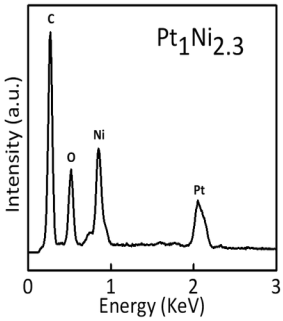

Extended Data Fig. 3| SEM-EDS analysis of Pt_{tet}@Ni(OH)$_2$. The SEM-EDS result of the Pt_{tet}@Ni(OH)$_2$ shows the Pt:Ni atomic ratio is around 1:2.3.

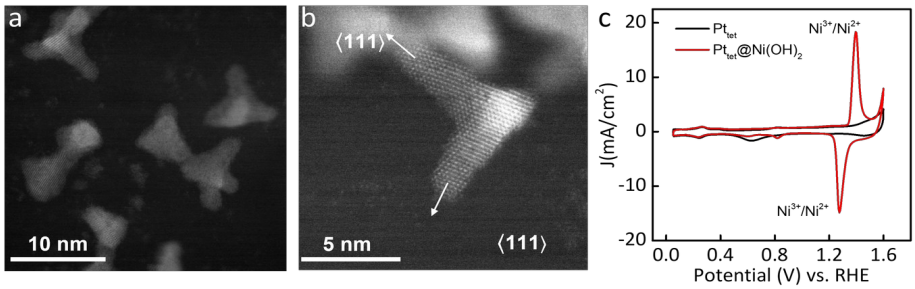

Extended Data Fig. 4| The Pt tetrapod core. a, Low-resolution STEM image of Pt tetrapods remained after completely removing the $Ni(OH)_2$ shell in acidic condition. **b,** The HAADF-STEM image of Pt tetrapod. The Pt core has a unique tetrahedral structure with four Pt pods grown along the <111> directions. **c,** The CV of $Pt_{tet}@Ni(OH)_2$ and Pt tetrapod. The redox peaks at 1.39 V vs. RHE in the anodic scan and 1.28 V vs. RHE in the cathodic scan represent the redox process of Ni^{3+}/Ni^{2+} on the surface of $Pt_{tet}@Ni(OH)_2$, while disappearing after in pure Pt_{tet}, indicating complete removal of the $Ni(OH)_2$ shell.

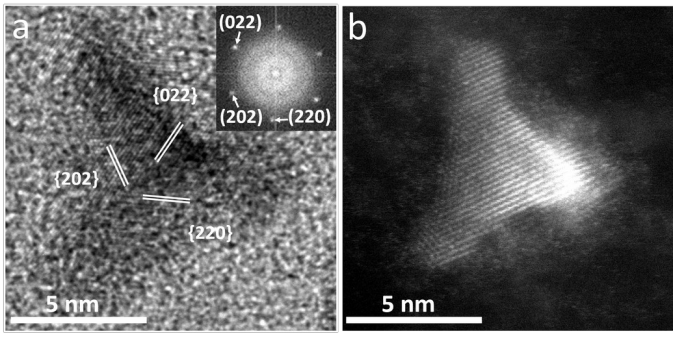

Extended Data Fig. 5| High-resolution TEM Characterization of Pt_{tet}@$Ni(OH)_2$. **a,** TEM images and FFT pattern of Pt_{tet}@$Ni(OH)_2$. Only the FFT pattern of Pt core can be observed and there is no FFT pattern of $Ni(OH)_2$, indicating the amorphous feature of $Ni(OH)_2$ shell. **b,** Representative HAADF-STEM images of Pt_{tet}@$Ni(OH)_2$. It can be overserved that the crystalline core is covered by a blurry amorphous shell.

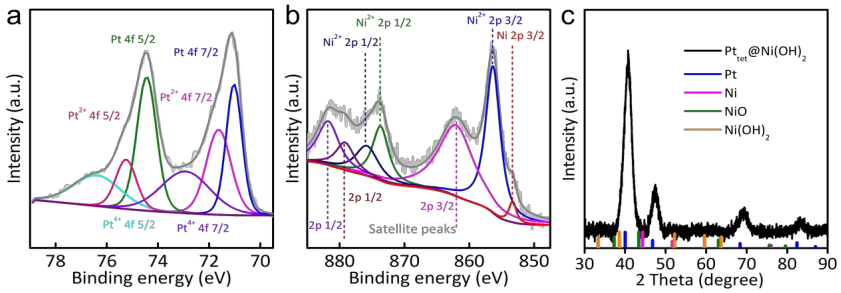

Extended Data Fig. 6| XPS and XRD characterization of Pt_{tet}@$Ni(OH)_2$. a, The Pt 4f XPS spectra of Pt_{tet}@$Ni(OH)_2$. Two main peaks at around 74.4 (Pt 4f5/2) and 71.1 eV (Pt 4f7/2) indicate that most of the Pt atoms are in the metallic phase. **b,** The Ni 2p XPS spectra of Pt_{tet}@$Ni(OH)_2$. The two main peaks at 856.1 eV and 873.7 eV belong to the $Ni(OH)_2$ 2p3/2 and $Ni(OH)_2$ 2p1/2 orbitals respectively, and the characteristic spin-energy separation of 17.6 eV between $Ni(OH)_2$ 2p3/2 and $Ni(OH)_2$ 2p1/2 is also in consist with other literature, delivering a clear result of $Ni(OH)_2$ dominated shell composition. The singlet feature of the $Ni(OH)_2$ 2p1/2 also strengthens the conclusion of $Ni(OH)_2$ as the main composition in the shell since the NiO 2p1/2 peak possesses a doublet peak feature. **c,** The XRD pattern of Pt_{tet}@$Ni(OH)_2$. Only symmetric peaks were found at 40.7° the XRD pattern of Pt_{tet}@$Ni(OH)_2$, which was assigned to the Pt-rich tetrapod skeleton. No $Ni(OH)_2$ peak was observed at around 37°.

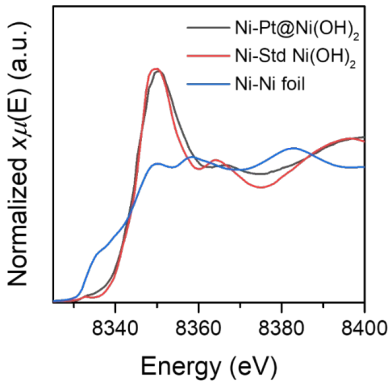

Extended Data Fig. 7| The Ni K-edge XANES experimental spectra of Pt_{tet}@$Ni(OH)_2$ along with reference materials. The oxidation state of Ni in Pt_{tet}@$Ni(OH)_2$ is slightly lower than the standard $Ni(OH)_2$, indicating the charge transfer at the interface from Pt to Ni.

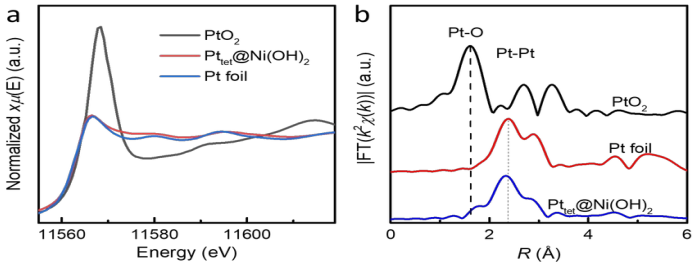

Extended Data Fig. 8| XAS results of Pt L3 edge. a, The Pt L_3-edge XANES experimental spectra. The Pt of Pt_{tet}@$Ni(OH)_2$ has a slightly higher oxidation state than the standard Pt foil, indicating the charge transfer from Pt to Ni at the interface, consistent with the Ni XANES spectra result. Note that the XAS signal is an average of all the targeted atoms, thus the change of XANES intensity resulting from the charge transfer between the interfacial atoms is diluted by the bulk signal from non-interfacial atoms, and thus is always not very obvious. **b,** Fourier transform magnitudes of the Pt L_3-edge EXAFS experimental signal of Pt_{tet}@$Ni(OH)_2$ along with reference materials.

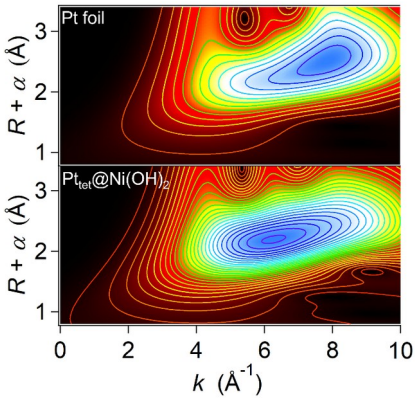

Extended Data Fig. 9| WT EXAFS signal of Pt and Pt foil. The negative shift of the maxima in the K space from Pt_{tet}@$Ni(OH)_2$ to Pt foil reveals that the Pt is coordinated with a lighter transition metal, which should be Ni in our case.

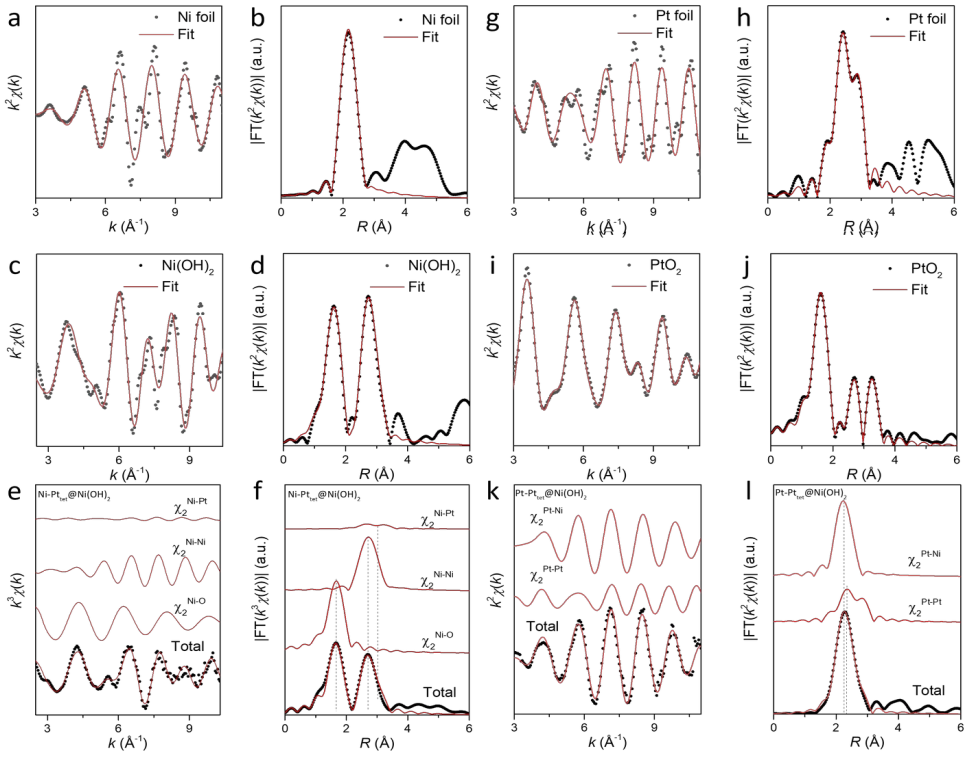

Extended Data Fig. 10| The Fourier-transformed magnitude of Ni K-edge EXAFS and Pt L-edge spectra in k and R space. a and **b,** Ni foil, **c** and **d,** $Ni(OH)_2$, and **e** and **f,** Ni K-edge $Pt_{tet}@Ni(OH)_2$. **g** and **h,** Pt foil. **i** and **j,**PtO_2. **k** and **l,** Pt L-edge $Pt_{tet}@Ni(OH)_2$. Measured and calculated spectra are well matched for all samples. The best-fit parameters are shown in Extended Data Tables 1 and 2.

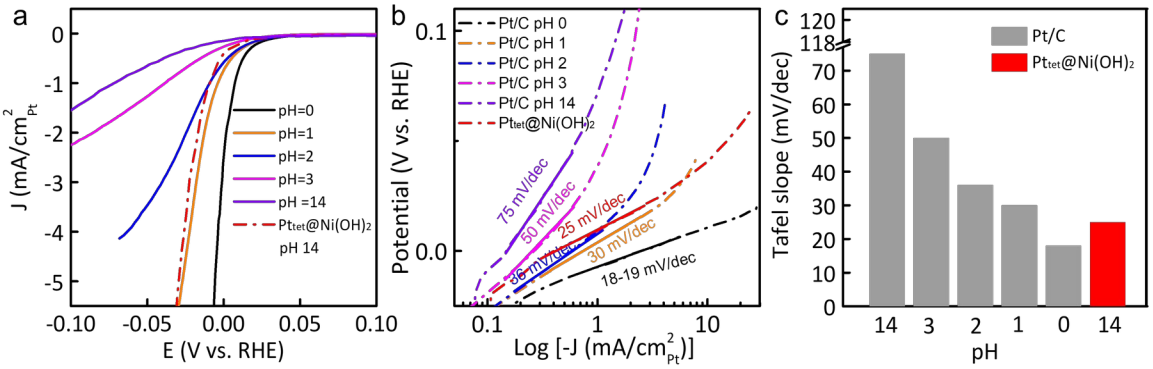

Extended Data Fig. 11| Kinetics comparison of $Pt_{tet}@Ni(OH)_2$ and Pt/C. a LSV curve of Pt/C at pH 0-3 and 14, and $Pt_{tet}@Ni(OH)_2$ at pH 14. The specific activity of $Pt_{tet}@Ni(OH)_2$ in pH 14 lies in between that of Pt/C in pH 1 and 3, indicating that the H^+ supply rate to the Pt core of $Pt_{tet}@Ni(OH)_2$ is close to the Pt/C in the pH 1-3. More specifically, its initial activity near the 0 V vs. RHE is slightly worse than that of pH 2, but it rapidly surpasses the pH 2 curve after 0.02 V vs. RHE, indicating that the overall H^+ supply rate at the high current level is even better than typical Pt/C under pH 2 and very close to pH 1. **b** and **c**,Tafel slope analysis of Pt/C at pH 0-3 and 14, and $Pt_{tet}@Ni(OH)_2$ at pH 14. The Tafel analysis shows that the Tafel slope of $Pt_{tet}@Ni(OH)_2$ is 25 mV/dec, higher than the 36 mV/dec of pH 2 and comparable to the 29 mV/dec of pH 1, indicating the HER kinetics of $Pt_{tet}@Ni(OH)_2$ is comparable to the Pt in pH 1. This further confirms our hypothesis that the $Ni(OH)_2$ shell can provide **an acidic-like hydrogen supply rate**, although not at the level of pH 0.

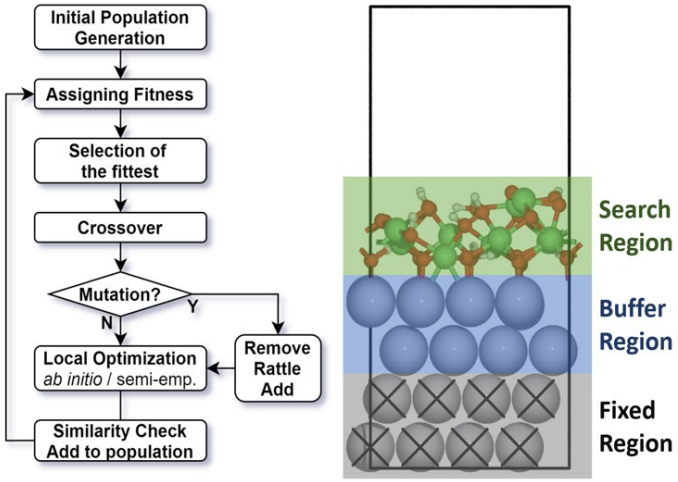

Extended Data Fig. 12| Workflow diagram and the model set-up of the GCGA search. A typical GCGA search consists of the following steps: (a) Defining the substrate slab, periodic boundary conditions, the search, buffer, and fixed regions, the types (and numbers) of species to sample, and their chemical potential. (b) Random generation of the initial candidates from Bond Length Distribution Algorithm (BLDA) followed by pre-optimization with Hookean potential to produce reasonable starting geometries. (c) Local optimization and energy evaluation of the candidates through the interface to VASP. (d) The fitness factor is assigned to each candidate based on the mating counts and the grand canonical free energy. (e) A similarity check against the current population is performed before adding any new candidate to remove duplicates. (f) Selection. The candidates with low fitness or unreasonable geometries are archived to maintain the population size. (g) Mating between the candidates alive to create offspring by the Split-and-splice operation, in which the parent slabs are cut along a random plane and then spliced together. In canonical GA search, the atoms farthest to the cutting plane will be removed to maintain the composition. Candidates with higher fitness are more probable to mate. (h) Mutation of the randomly chosen offspring by adding an atom, removing an atom, or rattling the surface atoms along random vectors drawn from a normal distribution. If an offspring is too similar to its parent, its mutation rate is raised to 100%. (i) Clustering and ranking all the optimized candidates after the GCGA run and report the low-energy configurations.

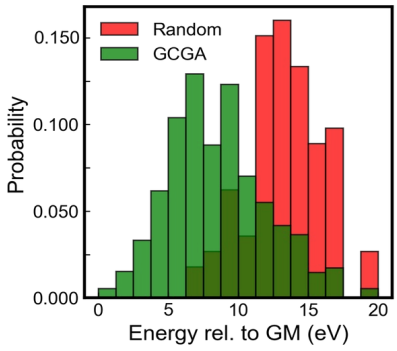

Extended Data Fig. 13| Histogram comparing the sampling efficiency of BLDA and GCGA in searching the low-energy surface states of the Pt@NiO_xH_y system. We applied the GCGA combined with DFT calculations to explore the structure of the Pt/ $Ni(OH)_2$ interface in an aqueous alkaline medium by applying a corresponding set of chemical potentials and relaxing the compositional degrees of freedom for O and H. In total, over unique 1200 structures are obtained after filtering and similarity check. The histogram of the energy distribution relative to the global minimum (GM) from random and GCGA samplings, relatively, and the geometry of the obtained GM structure. The GCGA methods sample much more efficiently into the low-energy region of the chemical subspace.

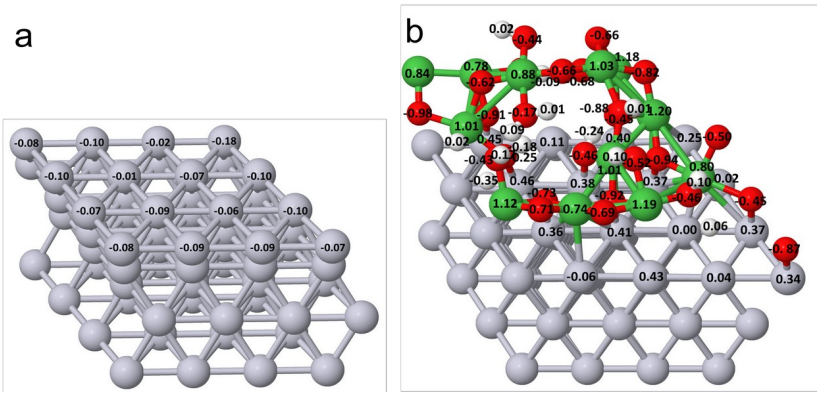

Extended Data Fig. 14| Bader charge of the surface atoms. **a,** The Bader charge of the surface atoms for Pt(111). **b,** The Bader charge of the surface atoms for Pt@NiOxHy. The values are labeled on the corresponding atom in the structural model, and units are in *e*. Compared with the Bader charge of surface atoms on Pt (111), The surface Pt atoms of Pt@NiOxHy are more positive, indicating the charge transfer from Pt to Ni. This is consistent with the XANES results and further proves the accuracy of our DFT model.

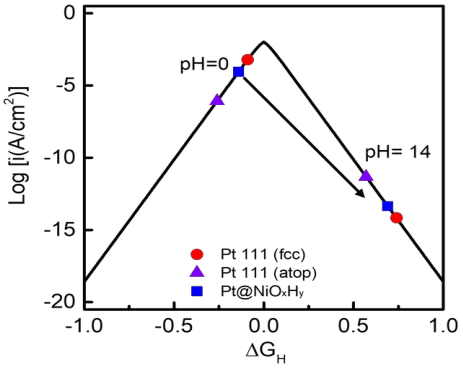

Extended Data Fig. 15| Volcano plot of HER exchange current density versus ΔG_H in logarithm scale. The positive shift of ΔG_H after changing the electrolyte from pH 0 to pH 14. The purple, red and blue dot mark the activity of Pt(111) atop, fcc and Pt@NiOxHy, respectively. The positive shift of ΔG_H to the other side of the volcano plot from pH 0 to pH 14 results in the deviation from the volcano top and thus the decrease of activity.

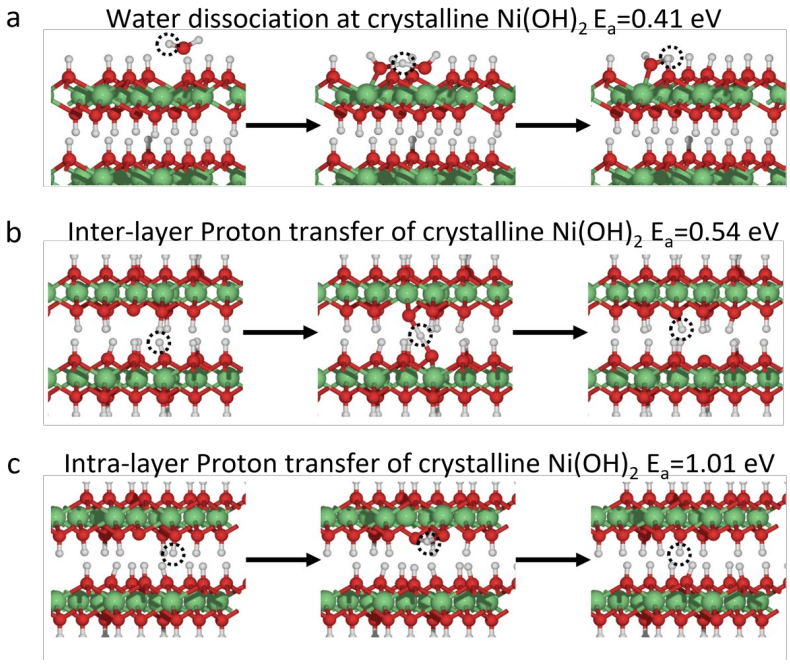

Extended Data Fig. 16| DFT calculation on proton transfer and water dissociation in the crystalline beta-Ni(OH)$_2$. a, The optimized geometries of the initial, transition, and final states of water dissociation in beta-Ni(OH)$_2$ with an activation barrier 0.41 eV; **b,** inter-layer proton transfer with an activation barrier of 0.54 eV; and **c,** intra-layer proton transfer with an activation energy barrier of 1.01 eV. Compared with the proton transfer activation barrier of 0.02 eV in the amorphous NiO_xH_y model, the proton transport in the crystalline Ni(OH)$_2$ is forbidden.

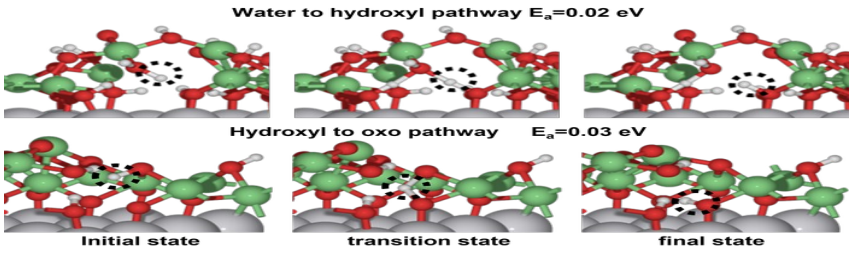

Extended Data Fig. 17. Geometries of the reaction profile for proton transfer via pathway and hydroxyl to oxo pathway, with activation energy of 0.03 eV.

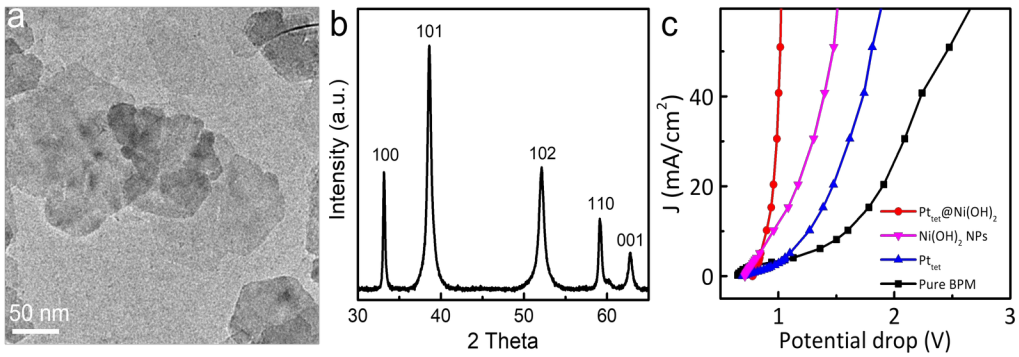

Extended Data Fig. 18| a, TEM image of crystalline $Ni(OH)_2$ nanoplate. **b,** XRD pattern of crystailline $Ni(OH)_2$ nanoplate. **c,** The water dissociation rate of Pt_{tet}, Pt_{tet}@$Ni(OH)_2$, crystalline $Ni(OH)_2$ nanoplates and pure BPM measured from BPM-based water electrolysis. The pure BPM with no catalyst, with the naked Pt_{tet} core or crysalline $Ni(OH)_2$ nanoplates catalysts require the overpotential of 1.64 V, 0.97 V, and 0.64 V, respectively, to reach the 50 mA/cm^2, while that with the amorphous $Ni(OH)_2$ shell (in Pt_{tet}@$Ni(OH)_2$) only needs 0.18 V overpotential to reach 50 mA/cm^2, demonstrating a much faster WD kinetics, and experimentally confirming that $Ni(OH)_2$ is the primary contributor to the WD, and the amorphous $Ni(OH)_2$ shell is more active for WD..

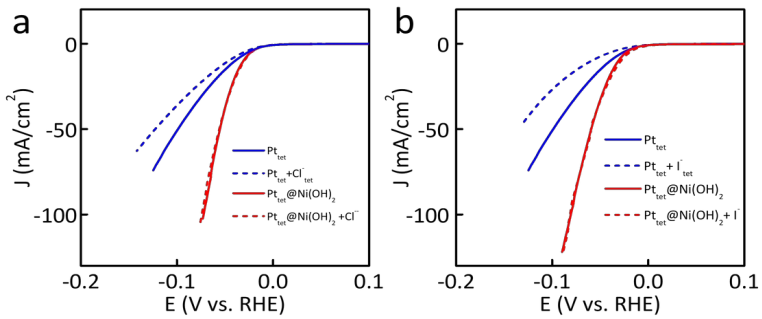

Extended Data Fig. 19| The Cl^- and I^- tolerance of Pt_{tet} and Pt_{tet}@$Ni(OH)_2$. a, in 0.5 M Cl^- and **b,** 0.25 M I^-, the pure Pt_{tet} has a significant activity drop, while there is no obvious change of Pt_{tet}@$Ni(OH)_2$ HER activity.

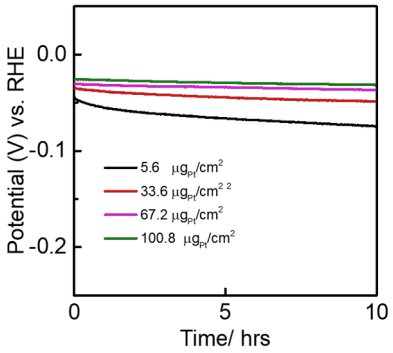

Extended Data Fig. 20| The stability test of Pt_{tet}@$Ni(OH)_2$ with a loading of 5.6, 33.6, 67.2 and 100.8 $\mu g_{Pt}/cm^2$. There is an obvious stability enhancement as loading increases.

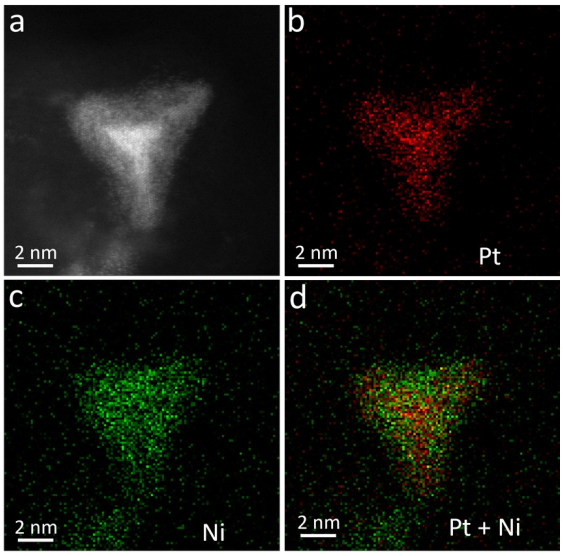

Extended Data Fig. 21| STEM image and EDS mapping of Pt_{tet}@$Ni(OH)_2$ after stability test. Both the structure and elements distribution are well maintained after the stability test.

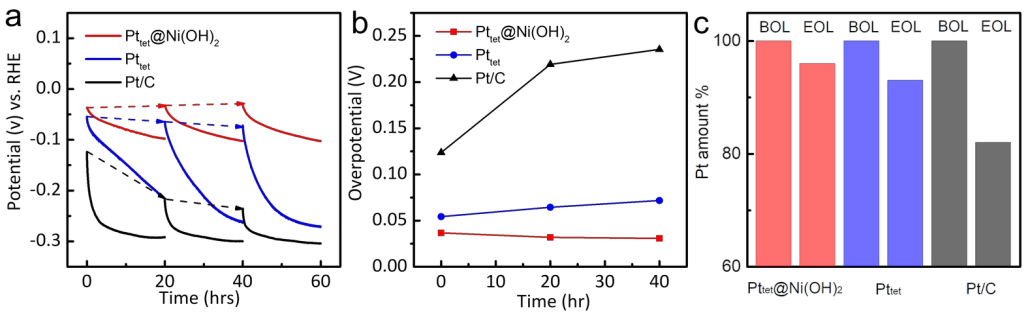

Extended Data Fig. 22| HER Stability test of Pt_{tet}@Ni(OH)$_2$ with periodic interval surface cleaning. a, Chronopotentiometry stability tests of Pt_{tet}@Ni(OH)$_2$, Pt_{tet} and Pt/C with periodic surface cleaning. A 30-cycle CV from 0.05 to 1.1 V vs. RHE was performed in between two stability tests to clean the surface. **b,** Irreversible overpotential increase of Pt_{tet} and Pt/C after periodic surface cleaning. The activity of Pt_{tet}@Ni(OH)$_2$ can be largely recovered after surface cleaning in repeated cycling test, indicating that the activity degradation of the Pt_{tet}@Ni(OH)$_2$ during the HER stability test is mostly due to the accumulation of H_2 bubbles that cover the Pt sites or other modification of local environment, with very little catalyst degradation. Nonetheless, more severe irreversible degradations are observed in Pt_{tet} and Pt/C control samples, in which the degraded activity can only be partially recovered with the CV scan to 1.1 V, further confirming the high durability of Pt_{tet}@Ni(OH)$_2$ with Ni(OH)$_2$ shell protection **c, Pt percentage loss before and after stability test. BOL: beginning of life; EOL: end of life**. The Pt_{tet}@Ni(OH)$_2$ catalyst only show <4% Pt loss, which may be largely attributed to the detachment of some nanoparticles when the electrode was initially immersed into the electrolyte because the activity can be fully recovered after surface cleaning in the repeated cycling test. The loss for Pt_{tet} and Pt/C is about 7% and 15% respectively, further confirming that the Ni(OH)$_2$ can effectively reduce the Pt loss for enhancing stability

Extended Data Table 1| Comparison of the Tafel slope of Pt_{tet}@$Ni(OH)_2$ in this work with the state-of-the-art literature.

	Material	Tafel slope (mV/dec)	Pontential range (mV vs. RHE)	Electrolyte	Ref
1	Pt_{tet}@$Ni(OH)_2$	**25**	10 to -20	1.0 M KOH	This work [a]
	Pt_{tet}	40	10 to -20		
		102	-50 to -100		
	Pt/C	75	-100 to -160		
		183	0 to - 50		
2	PtNi-O	40	10 to -20	1.0 M KOH	4[b]
3	SANi-Pt	37	10 to -20	1.0 M KOH	43[b]
4	Ni_3N-Pt	36.5	0 to -50 mV	1.0 M KOH	44
	Pt/C	50.6	0 to -50 mV		
5	$Pt_{3.21}Ni@Ti_3C_2$	38.5	20 to -20 mV	0.1M KOH	45
	Pt/C	39.5	20 to -20 mV		
6	1.9 nm Pt island	69	-10 to -20 mV	1.0 M KOH	46
7	D-PtNi/C	55	-5 to -25 mV	1.0 M KOH	47
	Pt/C	56	-5 to -25 mV		
8	NiS_2/PtNi NWs	20	-10 to -20 mV	**0.1 M $HClO_4$**	48
		38	-10 to -20 mV	0.1 M KOH	

[a]The Pt_{tet}@$Ni(OH)_2$ coreshell catalysts show a Tafel slope notably smaller than those of naked Pt_{tet}, commercial Pt/C, and all previously reported surface decorated Pt catalysts alkaline HER, demonstrating that this full encapsulation of Pt surface with proton permeable $Ni(OH)_2$ shell effectively isolates the Pt surface from the alkaline electrolyte and create a lower local pH on Pt surface, and thus fundamentally altering the HER pathway to acidic-like kinetics with the Tafel step limited pathway, achieving a much lower Tafel slope (< 30 mV/dec) and much higher activity.

[b]The Tafel slope is obtained from the recalculation from the original data in a different potential range compared with the value reported in the published version.

Extended Data Table 2| Ni K-edge EXAFS curve fitting parameters.[a]

sample	path	N	R (Å)	σ^2 (Å^2)	ΔE_0 (eV)	R, %
Ni foil[b]	Ni−Ni	12	2.48	0.008	0.5	0.01
$Ni(OH)_2$[c]	Ni−O Ni−Ni	6 6	2.06 3.11	0.008 0.008	-7.8	0.6
Ni-$Pt_{tet}(OH)_2$[c]	Ni−O Ni−Ni Ni−Pt	5.5 5.0 1.0	2.07 3.05 3.10	0.009 0.010 0.010	5.4	0.3

[a] N, coordination number; R, the distance between absorber and backscatter atoms; σ^2, Debye-Waller factor to account for both thermal and structural disorders; ΔE_0, inner potential correction; R factor (%) indicates the goodness of the fit. Error bounds (accuracies) that characterize the structural parameters obtained by EXAFS spectroscopy were estimated as N ± 20%; R ± 1%; σ^2 ± 20%; ΔE_0 ± 20%. S_0^2 was determined from Ni foil fitting. Bold numbers indicate fixed coordination number (N) according to the crystal structure.

[b] Fitting range: $3.2 \leq k$ (/Å) ≤ 11.0 and $1.0 \leq R$ (Å) ≤ 3.0.

[c] Fitting range: $2.5 \leq k$ (/Å) ≤ 10.4 and $1.0 \leq R$ (Å) ≤ 3.4.

Extended Data Table 3| Pt L_3-edge EXAFS curve fitting parameters.[a]

sample	path	*N*	*R* (Å)	σ^2 (Å^2)	ΔE_0 (eV)	*R*, %
Pt foil[b]	Pt−Pt	12	2.76	0.004	6.8	0.01
PtO_2[c]	Pt−O1 Pt−Pt Pt−O2	6 6 12	2.02 3.10 3.70	0.005 0.006 0.010	4.2	0.02
Pt-Pt_{tet}@$Ni(OH)_2$[b]	Pt−Pt Pt−Ni	8.9 2.0	2.70 3.12	0.004 0.005	5.0	0.2

[a]*N*, coordination number; *R*, the distance between absorber and backscatter atoms; σ^2, Debye-Waller factor to account for both thermal and structural disorders; ΔE_0, inner potential correction; *R* factor (%) indicates the goodness of the fit. Error bounds (accuracies) that characterize the structural parameters obtained by EXAFS spectroscopy were estimated as *N* ± 20%; *R* ± 1%; σ^2 ± 20%; ΔE_0 ± 20%. S_0^2 was determined from Pt foil fitting and fixed. Bold numbers indicate fixed coordination number (*N*) according to the crystal structure.

[b]Fitting range: 3.0 ≤ *k* (/Å) ≤ 11.0 and 1.2 ≤ *R* (Å) ≤ 3.2.

[c]Fitting range: 3.0 ≤ *k* (/Å) ≤ 11.0 and 1.2 ≤ *R* (Å) ≤ 3.6.

Extended Data Table 4| Comparison of the coordination number and bond length fitted from EXAFS and simulated NiO_xHy model. Our model is in good accordance with the experimental results and further confirms the accuracy and the robustness of the following simulation results based on this model. The slight deviation of coordination number (N) should be ascribed to much smaller numbers of atoms of the modeled motif compared with the real structure.

Sample	Path	N_{XANES}	N_{theory}	R_{XANES} (Å)	R_{theory} (Å)
Pt@NixOy	Ni-O	5.50	5.17	2.07	2.08
	Ni-Ni	5.00	4.50	3.05	3.04
	Ni-Pt	1.00	2.17	3.10	3.10
	Pt-Pt	8.90	8.00	2.70	2.80
	Pt-Ni	2.00	1.67	3.12	3.14

Extended Data Table 5| ΔG_H^o of the Pt(111) fcc and atop, and Pt@Ni_xO_y.

Sample	ΔG_H^0	ΔG_H (pH 0)	ΔG_H (pH 14)
Pt(111) fcc	-0.09 eV	-0.09 eV	0.74 eV
Pt(111) atop	-0.26 eV	-0.26 eV	0.57 eV
Pt@NixOy atop	-0.14 eV	-0.14 eV	0.69 eV
			-0.04-0.41 eV (proton supply rate corrected)

Extended Data Table 6| Comparison of HER performance of the Pt_{tet}@$Ni(OH)_2$ in this work with state-of-the-art catalysts. Mass activity (normalized by Pt loading) and specific activity (normalized by ECSA) were compared.[a]

Catalysts	Mass activity at -70 mV vs. RHE ($mA/\mu g_{Pt}$)	Specific activity at -70 mV vs. RHE (mA/cm^2_{Pt})	ECSA (m^2/g) in 1 M KOH	Reference
Pt/C	0.75	0.98	76.4	This work
Pt_{tet}@$Ni(OH)_2$	**13.4**	**27.7**	**48.4**	This work
SANi-JPtNWs	11.8	10.7	106	43
PtNiO octahedra	7.23	14.8	48.8	4
Pt NWs/ SL-$Ni(OH)_2$	0.679	2.48	27.3	3
NiO_x/Pt_3Ni Pt_3Ni_3-NWs	2.59	NA	NA	18[b]
Pt_3Ni_2-NWs/S C	2.48	NA	NA	17[b]
$Pt_{3.6}$Ni-S NWs	4.37	NA	NA	6
D-PtNi/C	1.03	4.26	24.2	47
1.9 nm Pt-island on Ni	7.7	14.7	52	46[c]
PtNi5-0.3	2.36	11.8	20	52
Pt SAs-Ni/NiO	~10.7	NA	NA	54[b]

[a]Generally, overpotential, mass activity, and specific activity are three major descriptors when comparing the Pt catalysts' HER performance. However, the overpotential largely depends on the Pt-loading which varies substantially among literature, making it difficult to use overpotential as the activity descriptor without considering the Pt-loading. To alleviate the effect of Pt-loading, it is more appropriate to use the mass activity at certain overpotential (e.g. -70 mV vs. RHE) or the overpotential achieved at a given current density normalized by ECSA for comparing the practical HER activity of different noble metal catalysts in literature. Additionally, specific activity can provide a better description of the intrinsic HER activity of a given catalyst surface.

[b]In these cases, the mass activity values were recalculated based on the reported mass loading and the electrode geometric surface area normalized HER polarization curve provided in the literature.

[c]The electrochemistry characterizations are conducted in 0.1 M KOH in these cases, otherwise in 1 M KOH if not specified.

Amorphous nickel hydroxide proton sieve tailors local chemical environment on Pt surface for high-performance alkaline hydrogen evolution reaction

Chengzhang Wan[1,2], Zisheng Zhang[1], Juncai Dong[3], Mingjie Xu[4, 5], Heting Pu[1], Daniel Baumann[1], Zhaoyang Lin[1], Sibo Wang[1], Jin Huang[2], Aamir Hassan Shah[1], Xiaoqing Pan[4,5,6], Tiandou Hu[3], Anastassia N. Alexandrova*[1,7], Yu Huang*[2,7], Xiangfeng Duan*[1,7,]

[1]Department of Chemistry and Biochemistry, University of California, Los Angeles; California 90095, United States;[2]Department of Materials Science and Engineering, University of California, Los Angeles; California 90095, United States; [3]Beijing Synchrotron Radiation Facility, Institute of High Energy Physics, Chinese Academy of Sciences; Beijing, China; [4]Department of Materials Science and Engineering, University of California, Irvine; California 92697, United States; [5]Irvine Materials Research Institute, University of California, Irvine; California, 92697, United States; [6]Department of Physics and Astronomy, University of California, Irvine; California 92697, United State;. [7]California NanoSystems Institute, University of California, Los Angeles; California 90095, United States.

*Correspondence. xduan@chem.ucla.edu, yhuang@seas.ucla.edu, ana@chem.ucla.edu

Supplementary Notes

Table of Contents

1. The estimation of H^+ diffusion distance

The OH^- concentration in the pH 14 electrolyte is 1 mol/L, which equals 1 OH^- in 1.66 nm^3. An H^+ generated from the dissociation of an H_2O molecule on the Ni species can only diffuse away for about 1.18 nm (the cubic root of 1.66 nm^3) before encountering and reassociating with another OH^- from the bulk alkaline electrolyte. Based on this consideration, the diffusion distance of a free hydronium (H_3O^+) is estimated to be around 1.18 nm. This simple estimate suggests that on the Pt surface that is partially decorated with crystalline Ni species, only a small fraction of Pt atoms that are located within 1.18 nm from the Ni species can benefit from the enhanced water dissociation.

2. Tafel slope extraction

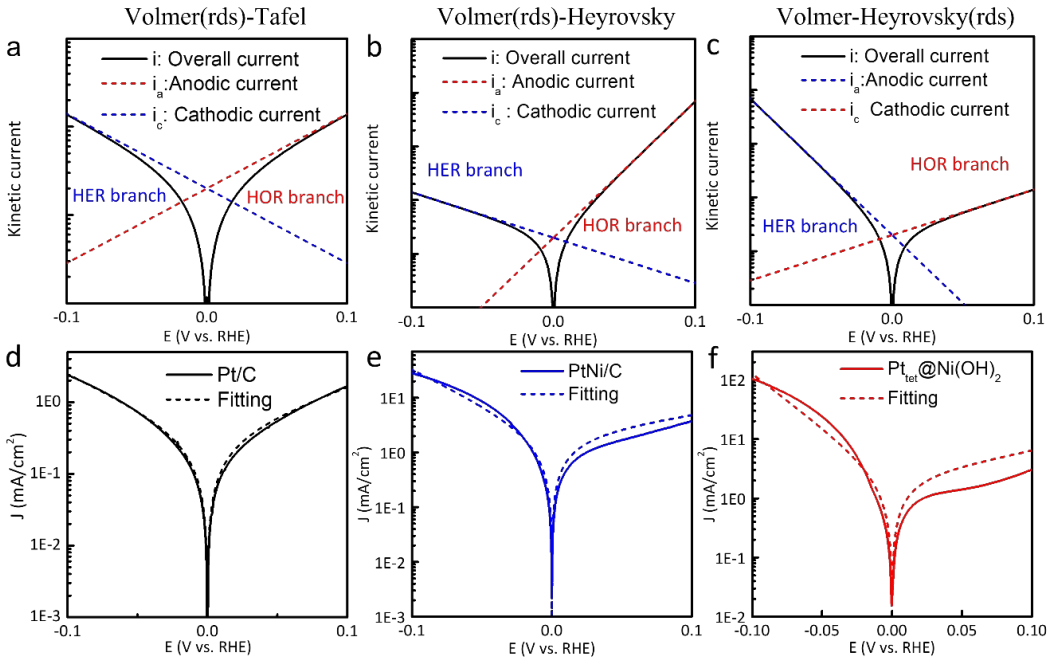

Fig. S1| The ideal polarization curve of HER/HOR branch for a, Volmer(rds)-Tafel pathway; b, Volmer(rds)-Heyrovsky pathway; and c, Volmer-Heyrovsky(rds) pathway. α=β=0.5 is used in the model. The HER branch represents the HER in the N_2 purged electrolyte. d, the B-V fitting results matched properly with the experimental polarization curves for Pt/C. The best B-V fitting results still cannot properly reconstruct the experimental polarization curves in the case of e, PtNi/C, and f, $Pt_{tet}@Ni(OH)_2$. (All the above tests are conducted under 1 M KOH, with N_2 purge and 1600 r.p.m. rotating speed).

The quantification and comparison of the Tafel slope is a nontrivial matter and requires extra caution to ensure a fair and consistent comparison. There are two commonly used methods to extract the Tafel slope from the HER polarization curve: (1) Butler-Volmer (B-V) fitting of the HER/ HOR kinetic current in the H_2 purged electrolyte; (2) linear fitting of the overpotential vs. logarithm of the HER kinetic current in the N_2 purged electrolyte. Both methods have been used in different literature. For the B-V fitting of Pt HER/HOR kinetic current under the H_2 purge, there are three possible ideal models depending on the exact rds:

i) Volmer (rds)-Tafel pathway, with the cathodic HER current $i_c = i_0 \times \left(-e^{\frac{-aF}{RT}\eta}\right)$ and the cathodic HOR current $i_a = i_0 \times \left(e^{\frac{\beta F}{RT}\eta}\right)$ (Fig. S1a);

ii) Volmer (rds)-Heyrovsky pathway, with the cathodic HER current $i_c = i_0 \times \left(-e^{\frac{-\alpha F}{RT}\eta}\right)$ and the anodic HOR current $i_c = i_0 \times \left(e^{\frac{(1+\beta)F}{RT}\eta}\right)$ (Fig. S1b);

iii) Volmer-Heyrovsky(rds) pathways, with the cathodic HER current $i_c = i_0 \times \left(-e^{\frac{-(1+\alpha)F}{RT}\eta}\right)$ and the anodic HOR current $i_c = i_0 \times \left(e^{\frac{\beta F}{RT}\eta}\right)$ (Fig. S1c);

where i_0 is the exchange current density, α and β are the symmetric factors) and are set to 0.5, R is the molar gas constant, T is the temperature and η is the potential. Through extensive studies with different types of HER catalysts, we found that the B-V fitting only works well for Pt/C with a moderate alkaline HER activity and standard Volmer (rds)-Tafel mechanism (Fig. S1c and d), while there are a number of critical issues in applying B-V fitting to the PtNi-based catalysts such as PtNi/C and the Pt_{tet}@$Ni(OH)_2$ (Fig. S1e and f). Specifically, Pt/C typically shows symmetric HER/HOR branches, and the kinetic current (i_k) can be well fitted with the B-V equation with an α value close to 0.5 in 1 M KOH (Fig. S1a). On the other hand, for PtNi/C and Pt_{tet}@$Ni(OH)_2$, due to the existence of surface Ni species, the HER rates are considerably enhanced while the HOR shows an abnormal passivation region at around 10-50 mV vs. RHE (Fig. S1e, f), leading to highly asymmetric HER/HOR branches that deviate from the standard expression of HER/HOR kinetics current. We hypothesize that the surface $Ni(OH)_2$ plays a different role in determining the activation energy for HER and HOR, and thus reduces their reversibility. As a result, the i_k cannot be reliably fitted with the B-V equation (Fig. S1e, f), and an attempted fitting could lead to unphysical α and β values (*e.g.*, α>1, or α+β ≠ 1), making it unreliable to derive or compare the Tafel slope. Additionally, we note there are also no strict rules for selecting the proper potential window when applying the B-V fitting. More active catalysts could reach mass transfer limitation at a lower overpotential, leading to a much smaller potential window that can be used for B-V fitting and thus higher uncertainty in the fitting results. Pt_{tet}@$Ni(OH)_2$ is clearly the case here due to its high activity.

Due to the above challenges associated with B-V fitting under H_2 purge, we have chosen to use the linear fitting of the N_2 purged HER curve, which has been widely used by other literature[1,2] to extract the Tafel slope for the following reasons: (i) Under the N_2 purging and high

rotating speed (1600 r.p.m.), the HOR branch is removed and thus linear fitting near the onset overpotential is not significantly affected by the HOR signal. There is a clearly linear region in the Tafel plot where the Tafel slope can be extracted. (ii) The Tafel slopes of different catalysts were extracted at similar current densities to ensure a similar mass transfer effect.

Lastly, we recognize there could be some level of uncertainties associated with the Tafel slope derivations. Nonetheless, a careful analysis reveals a substantially lower Tafel slope (27 mV/decade) is achieved in Pt_{tet}@$Ni(OH)_2$ in the alkaline electrolyte when compared with all other references (>36 mV/decade), which is fully validated by our internal control samples tested and evaluated with the exactly the same method. The difference is clearly beyond derivation uncertainties. Furthermore, it is important to note that our materials also deliver a record-high specific activity and a record-high mass activity, which is a directly measured number with less ambiguity. Together, our comprehensive evaluation and analysis robustly demonstrated that our unique design has enabled a superior HER catalyst in the alkaline electrolyte.

References

1. Ledezma-Yanez, I. *et al.* Interfacial water reorganization as a pH-dependent descriptor of the hydrogen evolution rate on platinum electrodes. *Nature Energy* **2**, 17031 (2017).

2. Monteiro, M. C. O., Goyal, A., Moerland, P. & Koper, M. T. M. Understanding Cation Trends for Hydrogen Evolution on Platinum and Gold Electrodes in Alkaline Media. *ACS Catalysis* **11**, 14328-14335 (2021).